GEOPHYSICS, VOL. 85, NO. 6 (NOVEMBER-DECEMBER 2020); P. H97–H113, 17 FIGS., 9 TABLES.
10.1190/GEO2019-0754.1

Joint inversion of full-waveform ground-penetrating radar and electrical resistivity data: Part 1

Diego Domenzain[1], John Bradford[2], and Jodi Mead[1]

ABSTRACT

We have developed an algorithm for joint inversion of full-waveform ground-penetrating radar (GPR) and electrical resistivity (ER) data. The GPR data are sensitive to electrical permittivity through reflectivity and velocity, and electrical conductivity through reflectivity and attenuation. The ER data are directly sensitive to the electrical conductivity. The two types of data are inherently linked through Maxwell's equations, and we jointly invert them. Our results show that the two types of data work cooperatively to effectively regularize each other while honoring the physics of the geophysical methods. We first compute sensitivity updates separately for the GPR and ER data using the adjoint method, and then we sum these updates to account for both types of sensitivities. The sensitivities are added with the paradigm of letting both data types always contribute to our inversion in proportion to how well their respective objective functions are being resolved in each iteration. Our algorithm makes no assumptions of the subsurface geometry nor the structural similarities between the parameters with the caveat of needing a good initial model. We find that our joint inversion outperforms the GPR and ER separate inversions, and we determine that GPR effectively supports ER in regions of low conductivity, whereas ER supports GPR in regions with strong attenuation.

INTRODUCTION

Imaging electrical properties (e.g., electrical permittivity ϵ and conductivity σ) are widely used for environmental and engineering applications. Contrasts in subsurface permittivity have been used to locate contaminant media (Bradford and Deeds, 2006; Babcock and Bradford, 2015), determine the availability of water in the subsurface (Benedetto, 2010; Dogan et al., 2011; Parsekian et al., 2012), measure stratigraphy and volumetric water content in snow (Bradford et al., 2009; Sold et al., 2013; Schmid et al., 2014), find geologic structures (Kjær et al., 2018), and build hydrogeologic models for water-flow simulations (Knight, 2001). Subsurface conductivity has been used to quantify water content (Binley et al., 2002; Brunet et al., 2010; Beff et al., 2013), determine temperature distributions for geothermal exploration (Fikos et al., 2012; Hermans et al., 2012; Spichak and Zakharova, 2015), assess risk of landslides (Jomard et al., 2010; Perrone et al., 2014), monitor carbon-dioxide storage (Bergmann et al., 2012; Carrigan et al., 2013), and characterize mountain permafrost (Hauck et al., 2003; Scapozza et al., 2011; Rödder and Kneisel, 2012). Despite the broad range of applications for mapping electrical properties of the subsurface using ground-penetrating radar (GPR) and electrical resistivity (ER) methods, often a choice has to be made in using either method because of their contrasting sensitivities.

GPR is sensitive to electrical permittivity through reflectivity and velocity, and it is also sensitive to electrical conductivity through reflectivity and attenuation. However, if attenuation is strong in the media of interest, the observed waveforms might not contain enough information to image either the permittivity or the conductivity. ER is directly (and only) sensitive to electrical conductivity; however, if the media of interest has low conductivity, the measured data might not have enough information to give a meaningful image. Fortunately, GPR and ER data have a complementary relationship. GPR is sensitive to what ER is not (permittivity), and ER is directly sensitive to what GPR is only sensitive to by weak reflections and attenuation (conductivity). Moreover, GPR data give a higher spatial resolution image of the media of interest in contrast with the lower spatial resolution obtained with the ER data.

Even though ray-theory methods for processing GPR data might resolve important features of the imaged media (Holliger et al., 2001; Bradford, 2006; Bradford et al., 2009), the caveat of only using the infinite frequency approximation of the data can lead

Manuscript received by the Editor 19 November 2019; revised manuscript received 7 August 2020; published ahead of production 24 August 2020; published online 06 November 2020.
[1]Boise State University, 1910 W University Dr, Boise, Idaho 83725, USA. E-mail: diegodomenzain@u.boisestate.edu (corresponding author); jmead@boisestate.edu.
[2]Colorado School of Mines, 1500 Illinois St, Golden, Colorado 78713-8924, USA. E-mail: jbradford@mines.edu.

DOI:10.1190/geo2019-0754.1

to unsatisfactory results (Johnson et al., 2007; Linde and Vrugt, 2013). Babcock and Bradford (2015) present an inversion algorithm for recovering subsurface electrical parameters from GPR common-offset data. Although successful on common-offset GPR field data, their method is limited to a 1D subsurface geometry, depends on a priori knowledge of background subsurface electrical properties, and uses a global optimization scheme to compute parameter sensitivities. Alternatively, we use the intrinsic physics of the underlying governing equations. Moreover, we note that a priori knowledge of subsurface parameters is needed to overcome the lack of long-wavelength information inherent to common-offset data. In our method, we can obtain long-wavelength information directly from data through conventional velocity analysis methods. Introduced by Tarantola (1984) in the acoustic regime, full-waveform inversion (FWI) aims to recover subsurface parameters by deterministically optimizing the objective function while taking into account the entire waveform record.

FWI of electromagnetic data (Ernst et al., 2007a; Meles et al., 2010) has seen steady interest for recovering the electrical properties of the subsurface. Although many advances have been made for crosshole data (Ernst et al., 2007a; Meles et al., 2010; Klotzsche et al., 2014; Gueting et al., 2017), using FWI for multioffset surface-acquired GPR data in the presence of strong attenuative media remains an important challenge (Lavoué et al., 2014; Schmid et al., 2014). These optimization schemes vary from generalized inversion methods (Jazayeri et al., 2018) and stochastic methods (Liu et al., 2018), where the descent direction is found without explicitly taking into account the physics of wave propagation.

Lavoué et al. (2014) perform FWIs of GPR on two synthetic examples, one with sources and receivers surrounding the target media and another with sources and receivers at the surface. When the target media are surrounded by sources and receivers, they are able to recover accurate spatial resolution and values of the electrical parameters even when their starting models for permittivity and conductivity are homogeneous. However, when using surface-acquired data, the conductivity solution lacks accuracy and spatial resolution at shallow depths and it is almost insensitive to sharp contrasts at depth. Moreover, in this case, their starting models for permittivity and conductivity are a smoothed version of the true parameters, which assumes that a very accurate initial model is available. The sharp difference in the resolution of the recovered parameters between these two synthetic experiments can be attributed to the sparse illumination due to having just surface-acquired data and shows how ill-posed GPR FWI can be when the conductivity is not known a priori.

An important aspect of FWI is to invert for the source wavelet present in the data. Pratt (1999) uses a source-wavelet optimization routine within the FWI scheme based on a Wiener filter. This approach has since been successfully adopted for FWI GPR field data (Ernst et al., 2007a; Klotzsche et al., 2014). In this work, we assume that the source wavelet is known. This assumption does not affect our joint inversion scheme because the implementation of the Wiener filter is done outside the FWI gradient computation (Pratt, 1999; Ernst et al., 2007a; Klotzsche et al., 2014). In a field data scenario, the source wavelet scheme of Pratt (1999) can easily be added to our algorithm.

ER inversion methods using the full response of the measured electric field range in how the data sensitivities are computed and in how the discretized physics are solved (Loke and Barker, 1996; Spitzer, 1998; Ha et al., 2006; Pidlisecky et al., 2007; Domenzain et al., 2017). Overall, the advances of the method have evolved in more accurate discretization schemes and computationally cheaper inversion routines. Because of the inherent low-spatial and shallow-depth resolution of the ER data, sharp boundaries of the subsurface conductivity can be challenging to capture without external a priori knowledge of the subsurface or strong regularization (Hetrick and Mead, 2018).

To exploit the complementary sensitivities of the GPR and ER experiments, we implement an inversion algorithm that recovers the permittivity and conductivity of the media of interest by joining the sensitivities of conductivity from the GPR and ER data in each iteration of the inversion process. In what follows, we make the physical assumptions of an isotropic linear media in which Ohm's law holds, with no lateral variation in the y-coordinate, a constant magnetic permeability of μ_o, and frequency-independent electrical parameters.

In recent work regarding GPR FWI (Ernst et al., 2007a; Meles et al., 2010; Klotzsche et al., 2014; Lavoué et al., 2014; Gueting et al., 2017), it has been assumed that electrical conductivity is constant over a bandwidth of the radar signal and permittivity is frequency independent. Incorporating frequency-dependent attenuation for an FWI approach can be done as Xue et al. (2017), where the authors use a modified version of the wave equation (Zhu and Harris, 2014) and develop forward and adjoint operators that approximate the effects of frequency-dependent attenuation. This enforces a higher computational cost compared to assuming frequency-constant attenuation. Giannakis et al. (2015) develop a 3D finite-difference time-domain forward model for electromagnetic wave propagation that incorporates frequency-dependent parameters by convolving Debye relaxation mechanisms directly in the wave solver. Their forward model is capable of accurately predicting the behavior of electromagnetic fields with frequency-dependent parameters, but an FWI algorithm that accounts for the convolution of relaxation mechanisms is still to be developed.

Recovering frequency-dependent attenuation from surface-acquired GPR data can be done as in Bradford (2007). The method links the attenuation coefficient to a dispersion relation that is measurable in the GPR data. It is noted that this method does not account for intrinsic versus scattering attenuation because it does not take into account the full kinematics of the electromagnetic wave. It is also recognized that because of the inability of GPR data to recognize reflections due to velocity from reflections due to conductive media, recovering the full attenuation response requires additional low-frequency data. Using the full kinematic response of GPR on surface-acquired data to recover attenuation is a very ill-posed problem. As an example, see the results of Lavoué et al. (2014) on surface-acquired data.

We recognize that frequency-independent electrical parameters are generally not true in nature. However, Appendix A and Table 5 show that for a range of earth materials, the frequency dependence varies by a small factor (less than 5 in most cases), and that in cases in which the conductivity is large, the radar loses most of its signal due to attenuation. Assuming frequency-independent parameters forms a starting point for the evaluation of the algorithm and comprises a reasonable trade-off among the computation cost, field applications, the full use of the GPR waveform, and a lack of enforced assumptions of subsurface geometry and petrophysical models.

Joining data from different types of geophysical imaging methods holds the promise of reducing the nonlinearity of characterizing subsurface material properties (Ogunbo et al., 2018). Different approaches coupling the subsurface material properties as well as different algorithmic workflows have been developed to join different types of sensitivities (Moorkamp, 2017). Broadly, the material properties coupling can be done via a geologic structure (in which different material properties are assumed to share the same geometry [Haber and Oldenburg, 1997; Gallardo and Meju, 2003; Haber and Gazit, 2013]) or linked by petrophysical relationships (Ghose and Slob, 2006). More specifically, Linde et al. (2006) use GPR and ER crosshole data assuming structural similarities of electromagnetic properties and simplifying the physics of GPR to only use traveltimes. Our approach for joint inversion does not assume structural similarities and does not need petrophysical relationships because the GPR and ER data are physically linked through conductivity with Maxwell's equations. Moreover, we directly join the GPR and ER sensitivities on the same computational grid. We are able to increase the amplitude and spatial frequency resolution of the inverted electrical properties in a joint inversion compared with individual inversions of surface-acquired data. In this way, the GPR and ER optimization problems effectively regularize each other while honoring the physics.

Although our algorithm is presented in the 2D space, it can be extended to the 3D space by using 3D forward models and inversion routines. The choice for the 2D space was done for ease in computation. Moreover, in a field data scenario in which 2.5D assumptions hold true, GPR data transforms can be applied to use a 2D GPR FWI scheme (Bleistein, 1986; Ernst et al., 2007a). In the case of ER, forward models that take into account 2.5D exist (Dey and Morrison, 1979; Pidlisecky and Knight, 2008) and inversion routines that explicitly use a 2.5D forward model can be used (Domenzain, 2020).

This paper is Part 1 of a two-part series. In Part 1, the "GPR inversion" and "ER inversion" subsections develop the separate inversion schemes, and in the "Joint inversion" section, the method for joining the different sensitivities is described. In the "Examples" section, we give results from our method with two different synthetic scenarios for underground exploration of surface acquisition: (1) low conductivity and (2) high conductivity. All of our results have added noise in the GPR and ER data. In Part 2 (Domenzain et al., 2019), we enhance the accuracy of our algorithm and invert a more demanding synthetic model based on an alluvial aquifer.

INVERSION METHODS

GPR inversion

The physics of the 2D GPR experiment are given by the time-dependent Maxwell's equations (Ernst et al., 2007b; Meles et al., 2010):

$$\begin{pmatrix} \mu_o & 0 & 0 \\ 0 & \mu_o & 0 \\ 0 & 0 & \varepsilon \end{pmatrix} \begin{pmatrix} \dot{H}_z \\ -\dot{H}_x \\ \dot{E}_y \end{pmatrix} = \begin{pmatrix} 0 & 0 & \partial_x \\ 0 & 0 & \partial_z \\ \partial_x & \partial_z & 0 \end{pmatrix} \begin{pmatrix} H_z \\ -H_x \\ E_y \end{pmatrix} - \sigma \begin{pmatrix} 0 \\ 0 \\ E_y \end{pmatrix} + \begin{pmatrix} 0 \\ 0 \\ -J_y \end{pmatrix}, \tag{1}$$

where E_y is the electric field component in the y-direction, (H_x, H_z) are the magnetic field components in the x- and z-direction, J_y is the source term, ε is the electrical permittivity, μ_o is the magnetic permeability of free space, and σ is the electrical conductivity. The terms ε and σ are assumed to be constant in time and frequency-independent. Let ε_o denote the electrical permittivity of free space. From now on, we will refer to the relative permittivity $\varepsilon_r = \varepsilon/\varepsilon_o$ as permittivity. To keep the notation clean, we will refer to operators and variables in capital and lowercase letters, respectively, and so we refer to wavefield E_y as u. Table 1 gives a comprehensive list of the notation symbols used in this paper. We use a finite-difference time-domain method on a Yee grid (Yee, 1966) with perfectly matched layer (PML) boundary conditions (Berenger, 1996) to solve the discretized time-domain (Domenzain et al., 2017) version of equation 1, which for reference we write as

$$\begin{aligned} \mathbf{u} &= \mathbf{L}_w \mathbf{s}_w, \\ \mathbf{d}_w^s &= \mathbf{M}_w \mathbf{u}, \end{aligned} \tag{2}$$

where $\mathbf{L}_w$ denotes the discretized differential (time-marching) operator of equation 1, $\mathbf{u}$ is the electric field y component defined in space and time, $\mathbf{s}_w$ is the source term, $\mathbf{M}_w$ is the measuring operator, and $\mathbf{d}_w^s = \mathbf{M}_w \mathbf{u}$ is the data of the experiment, i.e., a common-source multioffset gather. The operator $\mathbf{M}_w$ formalizes the action of taking the data $\mathbf{d}_w^s$ (a 2D slice in time and receivers) from the 3D wavefield tensor $\mathbf{u}$ with the dimensions of time, length, and depth. Therefore, each source $\mathbf{s}_w$ gives rise to a multioffset shot gather $\mathbf{d}_w^s$.

From now on, $\varepsilon_r \geq 1$ and $\boldsymbol{\sigma} > 0$ will denote the frequency-independent electrical permittivity and conductivity distributions in the xz-plane and discretized as matrices of size $n_z \times n_x$, where n_x and n_z denote the number of nodes in the xz-plane discretization.

We formulate our GPR inversion algorithm by finding parameters ε_{r*} and σ_* that satisfy (Ernst et al., 2007b; Meles et al., 2010)

$$\{\varepsilon_{r*}, \boldsymbol{\sigma}_*\} = \arg\min \frac{1}{2} \left(\Theta_{w,\varepsilon_r}(\varepsilon_r; \mathbf{d}_w^o) + \Theta_{w,\sigma}(\boldsymbol{\sigma}; \mathbf{d}_w^o) \right), \tag{3}$$

where the subscript $*$ denotes the imaged parameters and $\mathbf{d}_w^o$ denotes all of the observed GPR data. We have

$$\Theta_{w,\varepsilon_r} = \frac{1}{n_s} \sum_s \Theta_{w,\varepsilon_r}^s, \tag{4}$$

where s indexes the sources, n_s denotes the total number of sources, and

$$\Theta_{w,\varepsilon_r}^s = \frac{\|\mathbf{e}_w\|_2^2}{\|\mathbf{d}_w^{o,s}\|_2^2}, \tag{5}$$

where $\mathbf{d}_w^{o,s}$ is the observed data for one source and $\mathbf{e}_w = \mathbf{d}_w^s - \mathbf{d}_w^{o,s}$ is the residual of the modeled and observed data. Equation 5 is the sum of the squared residuals for one source location (Tarantola, 1984; Ernst et al., 2007b; Meles et al., 2010). A similar expression for $\Theta_{w,\sigma}$ follows with the only difference between Θ_{w,ε_r} and $\Theta_{w,\sigma}$ being the order in the inversion scheme in which they are evaluated.

To find model updates $\Delta\boldsymbol{\sigma}_w$ and $\Delta\varepsilon_r$ that minimize Θ_w, we first obtain the gradients $\mathbf{g}_{w,\sigma}^s$ and $\mathbf{g}_{\varepsilon_r}^s$ of $\Theta_{w,\varepsilon_r}^s$ and $\Theta_{w,\sigma}^s$, respectively, following Meles et al. (2010) using an FWI approach,

DOI:10.1190/geo2019-0754.1

$$\mathbf{v}_w = \mathbf{L}_w \mathbf{e}_w(-t), \tag{6}$$

$$\mathbf{g}^s_{w,\sigma} = -\sum_t \mathbf{u}(-t) \odot \mathbf{v}_w(t) \cdot \Delta t, \tag{7}$$

$$\mathbf{g}^s_{\varepsilon_r} = -\sum_t \dot{\mathbf{u}}(-t) \odot \mathbf{v}_w(t) \cdot \Delta t, \tag{8}$$

where t denotes time, $(-t)$ denotes time reversed, $\odot$ denotes element-wise multiplication, $\dot{\mathbf{u}}$ denotes the time derivative of $\mathbf{u}$ (computed with in a finite-difference way), $\mathbf{v}_w$ is the adjoint wavefield (the back-propagation of errors), and Δt denotes the discretized time interval. As noted by Kurzmann et al. (2013), using the adjoint method introduces high-amplitude artifacts near the receivers that dominate the gradients. To remove these high amplitudes, we first multiply the gradients by a 2D Gaussian surface in the xz-plane centered at the source location. The bandwidth of the 2D Gaussian equals a wavelength where the wavelength is computed using the characteristic frequency of our survey and the velocity at the source location. We then apply a Gaussian low-pass space-frequency filter following Taillandier et al. (2009) with the choice of bandwidth so as to only allow wavelengths larger than or equal to the characteristic wavelength of the model. The updates are

$$\Delta\sigma_w = -\frac{1}{n_w}\sum_{s=1}^{n_w} \alpha^s_\sigma \mathbf{g}^s_{w,\sigma}, \tag{9}$$

$$\Delta\varepsilon_r = -\frac{1}{n_w}\sum_{s=1}^{n_w} \alpha^s_{\varepsilon_r} \mathbf{g}^s_{\varepsilon_r}, \tag{10}$$

where n_w is the number of GPR common-shot gathers and α^s_σ and $\alpha^s_{\varepsilon_r}$ are step sizes for each gradient.

Even with a true descent direction $-\mathbf{g}^s_{\varepsilon_r}$, finding $\alpha^s_{\varepsilon_r}$ can be a very ill-posed inverse problem by itself leading to negative step sizes, overshoot of the solution ε_{r*} or a very slow convergence. Overshooting the solution ε_{r*} can lead to our current values of ε_r to fall outside the velocity interval determined by the stability conditions of our finite-difference wave solver in time (Courant et al., 1967) and space (e.g., numerical dispersion).

For these reasons, we choose to compute the step size $\alpha^s_{\varepsilon_r}$ with a three-point parabola approximation of the objective function $\Theta^s_{w,\varepsilon_r}$ in the direction of its gradient (Wright and Nocedal, 1999). Each point used in the parabola approximation is the image of a perturbed permittivity $\hat{\varepsilon}_{r,i}$ under the objective function $\Theta^s_{w,\varepsilon_r}$,

$$\hat{\varepsilon}_{r,i} = \varepsilon_r \odot \exp(-\varepsilon_r \odot p_i \kappa_{\varepsilon_r} \cdot \mathbf{g}^s_{\varepsilon_r}), \quad i = 1, 2, 3, \tag{11}$$

where κ_{ε_r} is a positive real number and p_i is a fixed user defined percentage. The update in equation 11 is done in logarithmic scale to ensure positivity constraints (Meles et al., 2010). At each iteration and for each source, κ_{ε_r} is chosen automatically to enforce the perturbed permittivity to lie within a certain range of possible values, i.e., within the stability velocity interval imposed by our wave solver (Courant et al., 1967) and we choose κ_{ε_r} to be as large as possible. We leave the details of finding κ_{ε_r} in Appendix B. The values for each p_i are chosen to capture the shape of a parabola given our parameter domain. Because our domain is constrained by κ_{ε_r}, a value of $p_i = 1$ is the largest value permitted. We choose p_i for $1 \le i \le 3$ to be 0, 0.05, and 0.5. The value $p_1 = 0$ is taken because, at a given iteration, we already have a value of $\Theta^s_{w,\varepsilon_r}$ for the current permittivity (i.e., with no perturbation). The values 0.05 and 0.5 are chosen arbitrarily. We proceed by computing $\Theta^s_{w,\varepsilon_r}(\hat{\varepsilon}_{r,i}; \mathbf{d}^{o,s}_w)$ for $i = 1, 2, 3$ and then fitting a parabola through these points from which we analytically compute where the argument takes its minimum value: $\alpha^s_{\varepsilon_r}$.

The computational cost of finding $\alpha^s_{\varepsilon_r}$ imposes one extra run of our forward model (equation 2) from what is done by Ernst et al. (2007b) and Meles et al. (2010), but it proves to give more accurate values for the descent direction. We note that our search for κ_{ε_r} guarantees that the permittivity values always lie within the stability conditions of our wave solver: for the perturbations $\hat{\varepsilon}_{r,i}$ and for the updated ε_r.

Because GPR is only sensitive to conductivity through attenuation and weak reflections, in the case of strong attenuation, the GPR data might not have enough information to constrain a parabolic shape on $\Theta^s_{w,\sigma}$ in the vicinity of the current parameters. We find the step size α^s_σ by first finding the largest possible real number $\kappa_{w,\sigma}$ for which the perturbation in the direction of $-\kappa_{w,\sigma}\mathbf{g}^s_{w,\sigma}$ keeps the conductivity within a prescribed range of possible values. We then take a small percentage (in the order of 1%) of this value to be α^s_σ.

In late iterations, we find that the updates in equation 9 can lead to an oscillatory exploration of the solution space. To mitigate this effect, we impose a momentum m_{ε_r} (Rumelhart et al., 1986) to the descent direction $\Delta\varepsilon_r$,

$$\Delta\varepsilon_r \leftarrow \Delta\varepsilon_r + m_{\varepsilon_r}\Delta\varepsilon_{r,\bullet}, \tag{12}$$

where $\Delta\varepsilon_{r,\bullet}$ is the update of the previous iteration. The value of m_{ε_r} is kept constant throughout the inversion with a value of 25%.

At each iteration, the updates are done in logarithmic scale to enforce the physical positivity constraint on ε_r and σ (Meles et al., 2010),

$$\varepsilon_r \leftarrow \varepsilon_r \odot \exp(\varepsilon_r \odot \Delta\varepsilon_r), \tag{13}$$

$$\boldsymbol{\sigma} \leftarrow \boldsymbol{\sigma} \odot \exp(\boldsymbol{\sigma} \odot \Delta\boldsymbol{\sigma}_w). \tag{14}$$

As noted by Meles et al. (2010), if the conductivity and permittivity reflections vary significantly, it is not always convenient to compute the gradients and update under the same forward run. In lieu of this observation, in each iteration, we first compute equation 2, we then compute $\Delta\varepsilon_r$ and update ε_r, we then compute our synthetic data (equation 2) again, compute $\Delta\boldsymbol{\sigma}_w$ and update $\boldsymbol{\sigma}$. In total, for each iteration for one source, we compute equation 2 four times and equation 6 two times. This amounts to six forward models per iteration for all sources,

$$\text{GPR total time per iteration} = 6 \cdot \text{fwd}_w, \tag{15}$$

where fwd_w is the total amount of time for all GPR forward models.

Assuming the source wavelet is known for all sources in our GPR experiment, we give the algorithm for computing the updates $\Delta\varepsilon_r$ and $\Delta\sigma_w$ in Figure 1. The full GPR inversion algorithm is given in

Figure 3. The initialization of our algorithm consists in defining all constants used in our inversion and inputting a good initial guess for the permittivity and conductivity.

ER inversion

The physics of the 2D ER experiment are given by the steady-state Maxwell's equations, where Ohm's law holds (Pidlisecky et al., 2007),

$$-\nabla \cdot \sigma \nabla \varphi = \mathbf{i}(\delta(x - s_+) - \delta(x - s_-)), \tag{16}$$

where φ is the electric potential, $\mathbf{i}$ is the current intensity, $s_\pm$ is the source-sink location, and $\sigma > 0$ is the electrical conductivity. Note that under our assumptions, we are assuming that conductivity in equation 16 is the same as in equation 1. We write the discretized version of equation 16 as

$$\mathbf{L}_{dc}\boldsymbol{\varphi} = \mathbf{s}_{dc}, \quad \mathbf{d}^s_{dc} = \mathbf{M}_{dc}\boldsymbol{\varphi}, \tag{17}$$

where $\mathbf{L}_{dc}$ is the discretized differential operator of equation 16, φ is the electric potential (a vector of size $n_x n_z \times 1$), $\mathbf{s}_{dc}$ is the source term (a vector of size $n_x n_z \times 1$), $\mathbf{M}_{dc}$ is the measuring operator that computes observed voltages (a matrix of size $n_{\mathbf{d}^s_{dc}} \times n_x n_z$, where $n_{\mathbf{d}^s_{dc}}$ denotes the number of measured voltages), and $\mathbf{d}^s_{dc}$ is the data of the experiment for one source (a vector of size $n_{\mathbf{d}_{dc}} \times 1$). Rather than limiting our algorithm to a specific array configuration, the data $\mathbf{d}^s_{dc}$ can be any set of voltage readings for a given source-sink location.

We adapt the finite-volume method presented by Dey and Morrison (1979) to our 2D geometry to build the discretized operator $\mathbf{L}_{dc}$, a sparse banded matrix of size $n_x n_z \times n_x n_z$ whose entries are a function of $\boldsymbol{\sigma}$ and the boundary conditions. Neumann boundary conditions are applied on the air-ground interface, and Robin boundary conditions are applied in the subsurface (Dey and Morrison, 1979). By specifying Neumann boundary conditions on the air-ground interface and Robin boundary conditions in the subsurface, the matrix $\mathbf{L}_{dc}$ is directly invertible. The source vector $\mathbf{s}_{dc}$ is sparse having only ± 1 entries at the source and sink positions.

To directly compare the sensitivities of both experiments, we use the same discretized grid for the GPR and the ER forward models. The spacings $\Delta x, \Delta z$, and Δt are determined by the Courant-Friedrichs-Lewy condition (Courant et al., 1967) with a user-imposed interval of possible velocities in order for the GPR forward model to be numerically stable. In general, these discretization constraints can impose a fine computational grid. Second-order optimization methods on such grids can significantly increase the memory requirements, thus hindering the range of applications for our algorithm. Instead, we choose the gradient descent as a compromise between memory and GPR resolution.

We formulate our ER inversion algorithm by finding $\boldsymbol{\sigma}_*$ that satisfies

$$\boldsymbol{\sigma}_* = \arg\min \Theta_{dc}(\boldsymbol{\sigma}; \mathbf{d}^o_{dc}), \tag{18}$$

where $\mathbf{d}^o_{dc}$ is all of the ER data. Recall that $\boldsymbol{\sigma} > 0$. We have

$$\Theta_{dc} = \frac{1}{n_s}\sum_s \Theta^s_{dc}, \tag{19}$$

where s indexes the source, n_s denotes the total number of sources, and

$$\Theta^s_{dc} = \frac{\|\mathbf{e}_{dc}\|_2^2}{\|\mathbf{d}^{o,s}_{dc}\|_2^2}. \tag{20}$$

We denote $\mathbf{d}^{o,s}_{dc}$ as the observed data for one source and $\mathbf{e}_{dc} = \mathbf{d}^s_{dc} - \mathbf{d}^{o,s}_{dc}$ as the residual of the modeled and observed data. Equation 20 is the sum of the squared residuals for one source location. To find the model update $\Delta\boldsymbol{\sigma}_{dc}$ that minimizes Θ^s_{dc}, we first find the gradient $\mathbf{g}^s_{dc}$ of Θ^s_{dc} with respect to $\boldsymbol{\sigma}$. Let ∇_σ be the vector of size $1 \times n_x n_z$ whose entries are the partial derivatives with respect to $\boldsymbol{\sigma}$. We compute $\mathbf{g}^s_{dc}$ using the adjoint potential field $\mathbf{v}_{dc}$,

$$\mathbf{L}^{\mathrm{T}}_{dc}\mathbf{v}_{dc} = \mathbf{M}^{\mathrm{T}}_{dc}\mathbf{e}_{dc}, \quad \mathbf{g}^s_{dc} = \mathbf{S}_{dc}\mathbf{v}_{dc}, \tag{21}$$

where $\mathbf{g}^s_{dc}$ and $\mathbf{v}_{dc}$ are vectors of size $n_x n_z \times 1$ and $\mathbf{S}_{dc} = -((\nabla_\sigma \mathbf{L}_{dc})\varphi)^{\mathrm{T}}$ is a matrix of size $n_x n_z \times n_x n_z$. We leave the details of this derivation for Appendix C.

Similarly to $\mathbf{g}^s_{\varepsilon_r}$ and $\mathbf{g}^s_{w,\sigma}$, the gradient $\mathbf{g}^s_{dc}$ exhibits strong amplitudes near the sources and receivers. We use the approach of Taillandier et al. (2009) to filter out these artifacts by applying a low-pass space-frequency-domain Gaussian filter with a choice

a) Permittivity update $\Delta\varepsilon_r$ with GPR

- Loop over all sources.
  1. Compute $\mathbf{u}$, $\mathbf{d}^s_w$, $\mathbf{e}_w$ and $\Theta^s_{w,\varepsilon_r}$.
  2. Compute $\dot{\mathbf{u}}$, $\mathbf{v}_w$ and $\mathbf{g}^s_{\varepsilon_r}$.
  3. Damp high amplitudes of $\mathbf{g}^s_{\varepsilon_r}$ near the source location.
  4. Smooth $\mathbf{g}^s_{\varepsilon_r}$ in the space frequency domain.
  5. Normalize $\mathbf{g}^s_{\varepsilon_r}$ by its largest amplitude and compute $\alpha^s_{\varepsilon_r}$.
- Compute Θ_{w,ε_r} and,

$$\Delta\varepsilon_r = -\frac{1}{n_w}\sum_{s=1}^{n_w} \alpha^s_{\varepsilon_r}\,\mathbf{g}^s_{\varepsilon_r}.$$

- Apply *momentum*,

$$\Delta\varepsilon_r \leftarrow \Delta\varepsilon_r + m_\varepsilon\,\Delta\varepsilon_{r,\bullet}.$$

b) Conductivity update $\Delta\boldsymbol{\sigma}_w$ with GPR

- Loop over all sources.
  1. Compute $\mathbf{u}$, $\mathbf{d}^s_w$, $\mathbf{e}_w$ and $\Theta^s_{w,\sigma}$.
  2. Compute $\mathbf{v}_w$ and $\mathbf{g}^s_{w,\sigma}$.
  3. Damp high amplitudes of $\mathbf{g}^s_{w,\sigma}$ near the source location.
  4. Smooth $\mathbf{g}^s_{w,\sigma}$ in the space frequency domain.
  5. Normalize $\mathbf{g}^s_{w,\sigma}$ by its largest amplitude and compute α^s_σ.
- Compute $\Theta_{w,\sigma}$ and,

$$\Delta\boldsymbol{\sigma}_w = -\frac{1}{n_w}\sum_{s=1}^{n_w} \alpha^s_\sigma\,\mathbf{g}^s_{w,\sigma}.$$

Figure 1. Algorithms for computing the updates $\Delta\varepsilon_r$ and $\Delta\sigma_w$.

of radius so as to only allow wavelengths larger than or equal to the smallest source-receiver spacing.

Once the gradients for all sources have been computed, the update is

$$\Delta\boldsymbol{\sigma}_{dc} = -\frac{1}{n_{dc}}\sum_{s=1}^{n_{dc}} \alpha_{dc}^{s}\mathbf{g}_{dc}^{s}, \tag{22}$$

where n_{dc} is the number of ER experiments and α_{dc}^{s} is a particular step size for each $\mathbf{g}_{dc}^{s}$. The step-size computations are done following Pica et al. (1990), in which a perturbation $\hat{\sigma}$ of $\boldsymbol{\sigma}$ in the direction of the gradient $\mathbf{g}_{dc}^{s}$ is needed. We find the optimal perturbation parameter κ_{dc} such that

$$\hat{\boldsymbol{\sigma}} = \boldsymbol{\sigma}\odot\exp(-\boldsymbol{\sigma}\odot\kappa_{dc}\mathbf{g}_{dc}^{s}), \tag{23}$$

using the same algorithm (but separately) as with the GPR inversion. Similarly to the GPR permittivity sensitivity, we add a percentage in the order of 10% of the previous iteration update to the current update $\Delta\boldsymbol{\sigma}_{dc}$ to avoid an oscillatory search of the solution space (Rumelhart et al., 1986),

$$\Delta\boldsymbol{\sigma}_{dc}\leftarrow\Delta\boldsymbol{\sigma}_{dc} + m_{dc}\Delta\boldsymbol{\sigma}_{dc\bullet}, \tag{24}$$

where $\Delta\boldsymbol{\sigma}_{dc\bullet}$ is the update from the previous iteration and m_{dc} is kept constant throughout the inversion. At each iteration, the update is done in logarithmic scale to enforce the physical positivity constraint on σ,

$$\boldsymbol{\sigma}\leftarrow\boldsymbol{\sigma}\odot\exp(\boldsymbol{\sigma}\odot\Delta\boldsymbol{\sigma}_{dc}). \tag{25}$$

We give the algorithm for computing the update $\Delta\boldsymbol{\sigma}_{dc}$ in Figure 2. The full ER inversion algorithm is given in Figure 3. The initialization of our algorithm consists in defining all constants used in our inversion and inputting a good initial guess for conductivity. In total, for each iteration for one source, we compute equation 17 twice, and equation 21 once. This amounts to three forward models per iteration for all sources,

$$\text{ER total time per iteration} = 3\cdot\text{fwd}_{dc}, \tag{26}$$

where fwd_{dc} denotes the total amount of time for all of the ER forward models.

Table 1. Reference for the notation used in the discretized inverse problems.

Symbol	Meaning	Note
ε_r	Discretized electrical relative permittivity	Used for GPR and ER
σ	Discretized electrical conductivity	
$\mathbf{L}$	Discretized differential operator	
$\mathbf{s}$	Discretized source	
$\mathbf{M}$	Discretized measuring operator	
$\mathbf{d}$	Synthetic data	
$\mathbf{e}$	Residual of synthetic versus observed data	
Θ	Objective function	
$\mathbf{v}$	Discretized adjoint field	
$\mathbf{g}$	Gradient of the objective function	
α	Step size for $\mathbf{g}$	
κ	Perturbation parameter used to find α	
m	Momentum parameter	
$\mathbf{u}$	Electric wavefield on the y component	Only GPR
$\dot{\mathbf{u}}$	Finite-difference time derivative of $\mathbf{u}$	
$\hat{\varepsilon}_r$	Perturbed relative permittivity	
$\Delta\sigma_w$	GPR conductivity update	
$\Delta\varepsilon_r$	GPR permittivity update	
$\Delta\varepsilon_{r,\bullet}$	GPR permittivity update from the previous iteration	
$\boldsymbol{\varphi}$	Discretized electric potential	Only ER
$\mathbf{S}_{dc}$	The matrix $-((\nabla_\sigma\mathbf{L}_{dc})\varphi)^{\mathrm{T}}$	
$\hat{\sigma}$	Perturbed conductivity	
$\Delta\sigma_{dc}$	ER conductivity update	
$\Delta\sigma_{dc\bullet}$	ER conductivity update from previous iteration	
$\Delta\sigma$	Joint conductivity update	Used for the joint update
a_w	Weight to regulate $\Delta\sigma_w$	
a_{dc}	Weight to regulate $\Delta\sigma_{dc}$	
h	Weight to regulate a_w and a_{dc}	
c	Step size for $\Delta\sigma$	

[3]Note: Symbols common in the GPR and ER experiments are stripped from their subscripts to avoid clutter.

JOINT INVERSION

We formulate our GPR and ER joint inversion algorithm by finding parameters ε_{r*} and σ_* that satisfy

$$\{\boldsymbol{\varepsilon}_{r*},\boldsymbol{\sigma}_*\} = \arg\min\frac{1}{2}(\Theta_{w,\varepsilon_r}(\boldsymbol{\varepsilon}_r;\mathbf{d}_w^o) + \Theta_{w,\sigma}(\boldsymbol{\sigma};\mathbf{d}_w^o)) + \Theta_{dc}(\boldsymbol{\sigma};\mathbf{d}_{dc}^o). \tag{27}$$

Recall that $\varepsilon_r \geq 1$ and $\boldsymbol{\sigma} > 0$. We optimize equation 27 by joining the updates $\Delta\boldsymbol{\sigma}_w$ and $\Delta\boldsymbol{\sigma}_{dc}$ obtained by equations 9 and 22, respectively. Because $\Delta\boldsymbol{\sigma}_w$ and $\Delta\boldsymbol{\sigma}_{dc}$ generally vary in magnitude, in order for the updates to share their different spatial sensitivities, we first normalize them by their largest amplitude and then add them together with scalar weights a_w and a_{dc},

$$\Delta\boldsymbol{\sigma} = a_w\Delta\boldsymbol{\sigma}_w + a_{dc}\Delta\boldsymbol{\sigma}_{dc}, \tag{28}$$

then normalize $\Delta\boldsymbol{\sigma}$ by its largest amplitude and finally write

$$\Delta\boldsymbol{\sigma}\leftarrow c\Delta\boldsymbol{\sigma}, \tag{29}$$

where c is the geometric mean of the maximum amplitudes of $\Delta\boldsymbol{\sigma}_w$ and $\Delta\boldsymbol{\sigma}_{dc}$ prior to normalization. See Figure 4a for a summary of this procedure. The choices for weights a_w and a_{dc} are made with the paradigm of letting updates $\Delta\boldsymbol{\sigma}_w$ and $\Delta\boldsymbol{\sigma}_{dc}$ always contribute to $\Delta\sigma$ in proportion to their objective function value at a given iter-

ation: If the objective function value of one is smaller than the other, then the one with the smaller value should be more heavily weighted. The ad-hoc computation of a_w and a_{dc} is

$$a_w = \begin{cases} 1 & \text{if } h\Theta_{w,\sigma} \le \Theta_{dc} \\ \frac{1}{\sqrt{|h\Theta_{w,\sigma} - (\Theta_{dc}-1)|}} & \text{if } \Theta_{dc} < h\Theta_{w,\sigma}, \end{cases}$$

$$a_{dc} = \begin{cases} 1 & \text{if } \Theta_{dc} \le h\Theta_{w,\sigma} \\ \frac{1}{\sqrt{|h\Theta_{w,\sigma} - (\Theta_{dc}+1)|}} & \text{if } h\Theta_{w,\sigma} < \Theta_{dc}, \end{cases} \tag{30}$$

where h is a positive number that further regulates the relative weight of GPR versus ER sensitivities. The value of h modulates how much we weigh each sensitivity: An increasing value of h decreases the weighting of $\Delta\boldsymbol{\sigma}_w$, whereas a decreasing value of h increases the weighting of $\Delta\boldsymbol{\sigma}_w$.

Moreover, the choice of h over each iteration manages two aspects of the inversion: (1) At early iterations, GPR data give better sensitivity of sharp boundaries at shallow depths compared to ER data, so $\Delta\boldsymbol{\sigma}_w$ should be weighed more; however, at later iterations, ER data gives better sensitivity overall, so $\Delta\boldsymbol{\sigma}_w$ should be weighed less. (2) We interpret an increase of Θ_{dc} (or $\Theta_{w,\sigma}$) with respect to the last iteration as a "cry for help," so $\Delta\boldsymbol{\sigma}_w$ should be weighed less (or more). Figure 5 shows the expected "bowtie" shape over iterations of a_w and a_{dc} that drives the physical sensitivities of our data in the parameter-space search path. At early iterations, the GPR data first

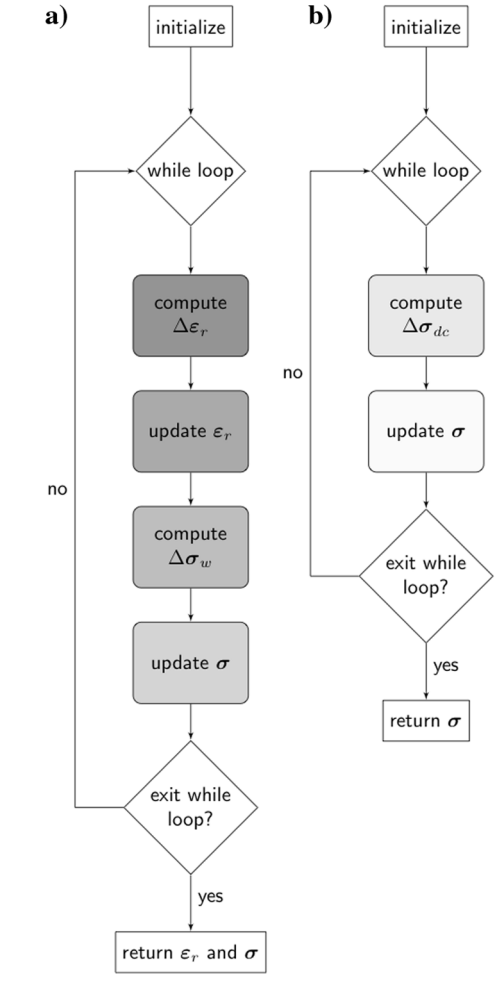

Figure 3. Inversion algorithms for (a) GPR and (b) ER.

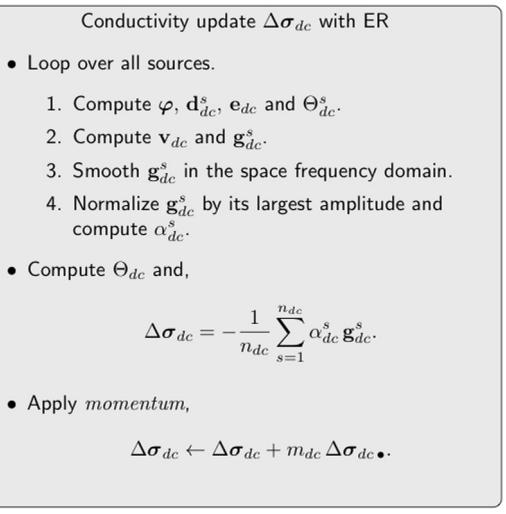

Figure 2. Algorithm for computing the update $\Delta\boldsymbol{\sigma}_{dc}$.

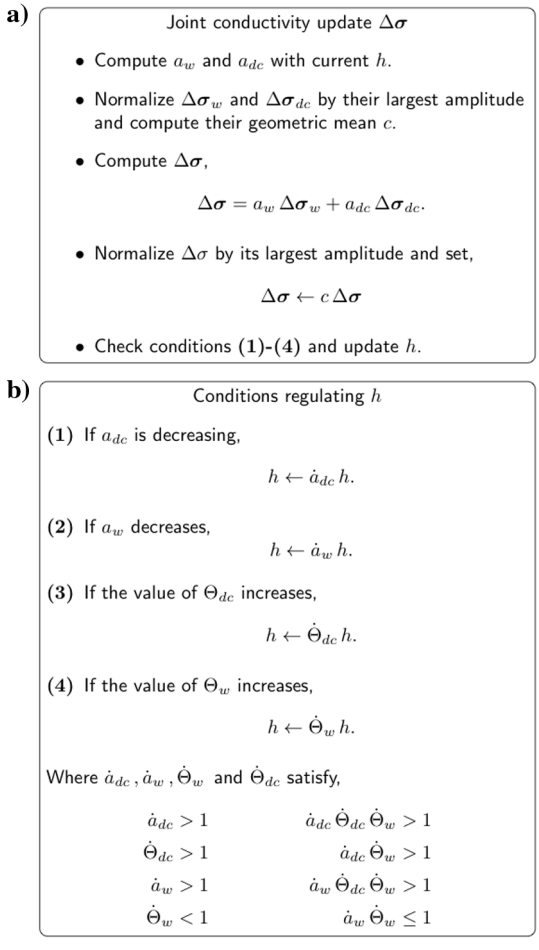

Figure 4. Algorithm for computing the update $\Delta\boldsymbol{\sigma}$ as explained in the "Joint inversion" section.

resolve the structure of the model, whereas the ER data struggle to resolve the conductivity at depth, so the weight a_w is given a larger value than a_{dc}. At later iterations, once the GPR data have resolved enough structure, the roles of a_w and a_{dc} are reversed.

Because the geometries of the hypersurfaces defined by $\Theta_{w,\sigma}$ and Θ_{dc} as a function of σ are not known, we ensure that the values of a_w and a_{dc} comply with the bowtie shape by enforcing emergent conditions (Cucker and Smale, 2007) that act individually on the magnitude of h, but when used together they interact into forming the bowtie shape. The conditions are (see Figure 4b)

(0) We first choose a value of a_{dc} for the first iteration to be positive and smaller than 1 and force the first choice of h to comply with this initial value of a_{dc}.
(1) As the iterations proceed, if a_{dc} is decreasing we increase h by a fixed ratio $\dot{a}_{dc}$,

$$h \leftarrow \dot{a}_{dc} h. \tag{31}$$

Note that a_{dc} can only decrease if a_w is 1.
(2) If a_w decreases, we further force the descent of a_w increasing h by a fixed ratio $\dot{a}_w$,

$$h \leftarrow \dot{a}_w h. \tag{32}$$

Note that the decrease of a_w begins when a_{dc} reaches 1.

To ensure that the "cries for help" are listened at each iteration, we enforce conditions (3) and (4) below.

(3) If the value of Θ_{dc} increases with respect to the last iteration, we increase h by a fixed ratio $\dot{\Theta}_{dc}$,

$$h \leftarrow \dot{\Theta}_{dc} h. \tag{33}$$

(4) If the value of $\Theta_{w,\sigma}$ increases with respect to the last iteration, we decrease h by a fixed ratio $\dot{\Theta}_w$,

$$h \leftarrow \dot{\Theta}_w h. \tag{34}$$

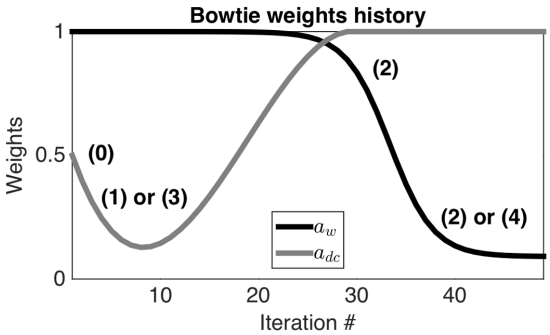

Figure 5. Diagram of weights a_w and a_{dc} as a function of the iterations. An initial value for a_{dc} is chosen following condition **(0)**. If a_{dc} decreases over the iterations or if Θ_{dc} increases, condition **(1)** or **(3)** is activated to increase a_{dc}. Once a_{dc} reaches the value of 1, a_w is forced to steadily decrease with condition **(2)**. If $\Theta_{w,\sigma}$ increases over the iterations, condition **(4)** is activated and a_w is increased but is regulated by condition **(2)**.

In summary, the weight h regulates the current iteration's choice of confidence over the sensitivities $\Delta\sigma_w$ and $\Delta\boldsymbol{\sigma}_{dc}$, whereas the weights $\dot{a}_{dc}$, $\dot{a}_w$, $\dot{\Theta}_{dc}$, and $\dot{\Theta}_w$ regulate how h changes over each iteration. From conditions **(1)–(4),** we have

$$\begin{aligned} \dot{a}_{dc} &> 1 \quad \dot{\Theta}_{dc} > 1 \\ \dot{a}_w &> 1 \quad \dot{\Theta}_w < 1. \end{aligned} \tag{35}$$

Because each condition **(1)–(4)** is tested at each iteration, more than one condition can be activated in the same iteration, although not all combinations are possible; for example, if **(1)** is activated, then **(2)** is not because a_{dc} descending implies that a_w is 1. Out of all the possible combinations of repeated conditions of **(1)–(4)**, only four are ambiguous in whether h increases or decreases; see equation 36. We solve the ambiguities involving the GPR and ER terms by imposing an increase on h when they occur because this gives a higher weight on $\Delta\boldsymbol{\sigma}_{dc}$, which is the update that is directly sensitive to the conductivity:

$$\begin{aligned} \dot{a}_{dc}\dot{\Theta}_{dc}\dot{\Theta}_w &> 1 \\ \dot{a}_{dc}\dot{\Theta}_w &> 1 \\ \dot{a}_w\dot{\Theta}_{dc}\dot{\Theta}_w &> 1 \\ \dot{a}_w\dot{\Theta}_w &\geq 1. \end{aligned} \tag{36}$$

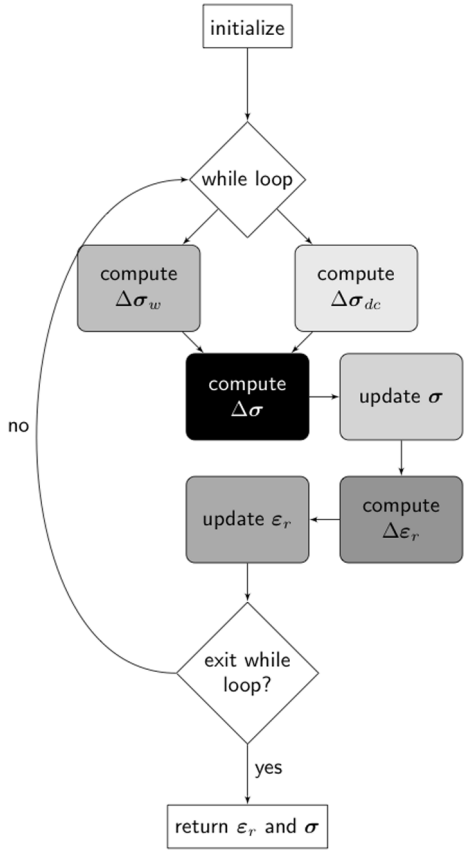

Figure 6. Joint inversion algorithm as explained in the "Joint inversion" section.

In practice, we treat h as an invisible variable and only worry about finding values for $\dot{a}_{dc}, \dot{a}_w, \dot{\Theta}_{dc}$, and $\dot{\Theta}_w$. which remain constant throughout the inversion. These values are found empirically. Table 2 holds the designated roles of values $\dot{a}_{dc}, \dot{a}_w, \dot{\Theta}_{dc}$, and $\dot{\Theta}_w$. Table 3 holds the values used in our inversions for the low- and high-conductivity scenarios.

The update for optimizing equation 27 is

$$\boldsymbol{\sigma} \leftarrow \boldsymbol{\sigma} \odot \exp(\boldsymbol{\sigma} \odot \Delta\boldsymbol{\sigma}). \tag{37}$$

We summarize the procedure of computing the joint update $\Delta\boldsymbol{\sigma}$ together with weight h in Figure 4. From equations 15 and 26, we compute the dominant terms for the total time per iteration for our joint inversion: six times the amount of time for the GPR forward model and three times the amount of time for the ER forward model for all sources,

$$\text{joint total time per iteration} = 6 \cdot \text{fwd}_w + 3 \cdot \text{fwd}_{dc}. \tag{38}$$

We note that the total time for our joint inversion is just the sum of the time taken by both inversions. In practice, we implement our inversions in parallel over the number of sources in our experiments. Because the times fwd_w and fwd_{dc} depend on the number of parallel CPUs available, we report the ratio of time required for just one forward model. For the examples presented in this work, one ER forward model costs 0.02 GPR forward models. Specifically, our inversions were computed on 20 cores running in parallel. One GPR iteration (updating $\boldsymbol{\epsilon}_r$ and $\boldsymbol{\sigma}$) takes 14 min, one ER iteration takes 40 s, and one joint iteration takes 15 min. Hence, the amount of time in the joint inversion is dominated by the GPR data by more than 93%. The full joint inversion algorithm is given in Figure 6.

Table 2. Parameters for our joint inversions that were found empirically and remained fixed throughout the inversions.

Parameter	Role	Turn-on
Initial a_{dc}	Initial weight on $\Delta\boldsymbol{\sigma}_{dc}$	Only in the first iteration
$\dot{a}_{dc}$	Increase h and a_{dc}	Only when $a_w = 1$
$\dot{a}_w$	Increase h, decrease a_w	Only when $a_{dc} = 1$
$\dot{\Theta}_{dc}$	Increase h, weigh $\Delta\boldsymbol{\sigma}_{dc}$ more	Always
$\dot{\Theta}_w$	Decrease h, weigh $\Delta\boldsymbol{\sigma}_w$ more	Always

[4]Note: An increase in h favors $\Delta\boldsymbol{\sigma}_{dc}$ more than $\Delta\boldsymbol{\sigma}_w$; conversely, a decrease in h favors $\Delta\boldsymbol{\sigma}_w$ more than $\Delta\boldsymbol{\sigma}_{dc}$.

Table 3. Inversion parameters used for the low- and high-conductivity scenario.

Parameter	Low $\boldsymbol{\sigma}$	High $\boldsymbol{\sigma}$
Initial a_{dc}	0.85	0.9
$\dot{a}_{dc}$	4	2
$\dot{a}_w$	2	1.5
$\dot{\Theta}_{dc}$	6	20
$\dot{\Theta}_w$	0.9	0.9

EXAMPLES

Subsurface models

We illustrate our algorithm with two possible scenarios of the subsurface: one with low conductivity ($\boldsymbol{\sigma}$ between 1 and 4 mS/m) and one with high conductivity ($\boldsymbol{\sigma}$ between 5 and 20 mS/m) as shown in Figure 7. The permittivity is kept equal (but is assumed unknown) in both scenarios. We place a box of size 1×1 m present in the permittivity and conductivity and a reflector at depth with a 1 m thickness present only in the permittivity.

Following the conditions given by Courant et al. (1967), we choose a discretization of $\Delta x = \Delta z = 0.017$ m and $\Delta t = 0.036$ ns. The discretized subsurface is a rectangle with $233 \times 1161 \approx 270 \times 10^3$ grid nodes. A 1 m thick air layer is further added to the GPR forward model and is then padded with a 1 m thick PML layer all around the domain. Because we are inverting for permittivity and conductivity, the total number of unknown parameters in our inversion is approximately 540×10^3.

We invert for permittivity and conductivity starting from homogeneous background models: $\sigma = 1$ mS/m and $\sigma = 4$ mS/m for

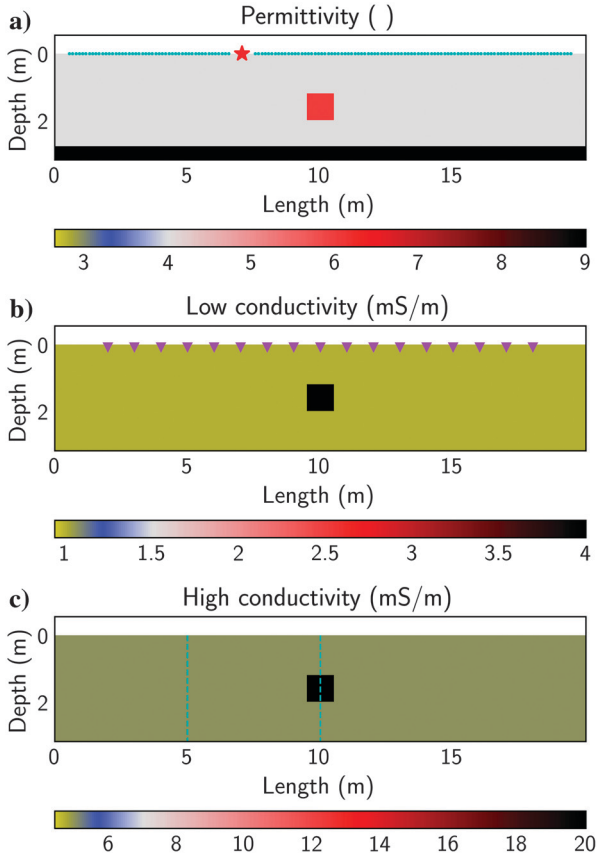

Figure 7. Subsurface models used for our inversions. The size of the box is 1×1 m. (a) The permittivity background, bottom reflector, and box have values of 4, 9, and 6, respectively. The conductivity background and box have values of 1 and 4 mS/m for the low conductivity (b) and 4 and 20 mS/m for the high conductivity (c), respectively. An example of the GPR receivers and source is depicted in cyan and red in (a). The ER electrodes are shown purple in (b). Borehole locations are shown in (c). The size of the discretized domain is approximately 270×10^3 grid nodes for a total of 540×10^3 unknown parameters.

the low- and high-conductivity scenarios, respectively, and $\varepsilon_r = 4$ for both scenarios.

We choose the same initial models for all inversions to compare their performance. Moreover, choosing the same initial model for our joint inversion enables the GPR and ER sensitivities to cooperatively search the solution space. If the initial conductivity model were to be accurately resolved by either data set, say, for example, the ER data, then the ER sensitivity might not have enough information to share with the GPR data. Furthermore, in this scenario, the GPR sensitivity to the conductivity might lack high-spatial frequency content, thus not aiding the ER sensitivity in finding a better solution.

The choice for the size of the box in our models is intended to stress our inversions as much as possible: large enough to have two wavelengths of the electromagnetic wave pass through, but small enough to be just within the minimum resolution of our ER acquisition sensitivity. The choice for the permittivity reflector aims to examine the inversion artifacts that may arise when the GPR data sensitivity to the subsurface differs from that of the ER data. We show the usefulness of the method on an exploration scenario with physical parameters relevant for field applications and simple enough for interpretation and assessment of our method.

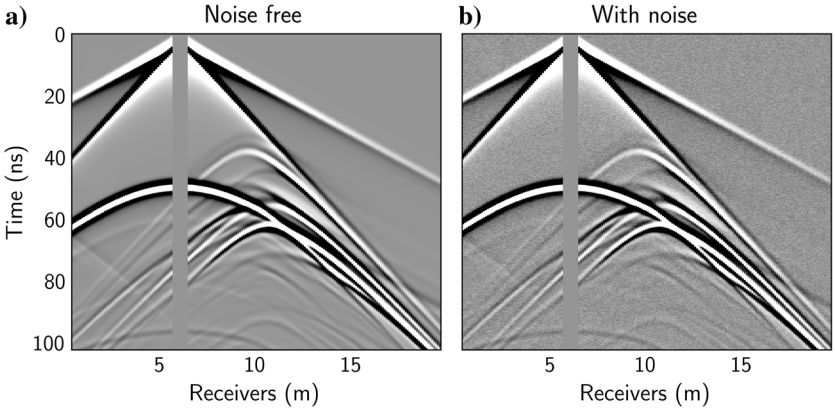

Figure 8. GPR data for one source noise free and with added noise for the low-conductivity example.

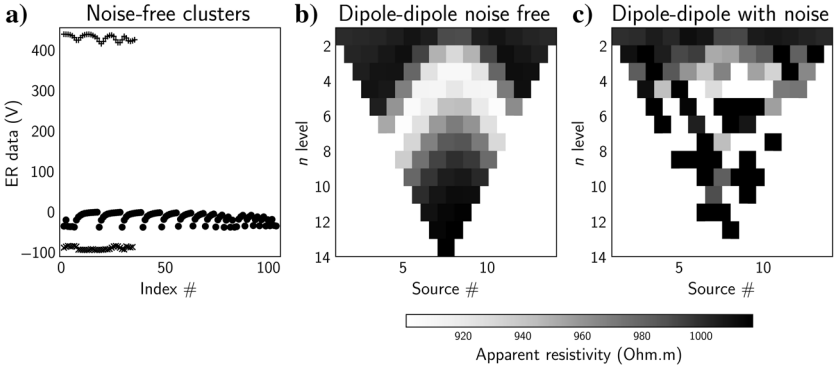

Figure 9. (a) All ER data noise free and the clusters used for adding noise depicted with symbols +, •, and ×. (b) Pseudosection of a dipole-dipole survey noise free and (c) with added noise.

Data acquisition

The GPR data are synthetically generated by applying 20 equally spaced sources (with a Ricker wavelet signature of 250 MHz) on the air-ground interface with the source-receiver spaced a wavelength away ($\asymp$0.5 m) and the receiver-receiver distance a quarter of a wavelength away all along the air-ground interface. Note that this acquisition scheme is multioffset for each source. Figure 7a shows an example for a source position at $x = 7$m and receivers along the surface. The source wavelet is assumed known throughout the inversion.

The ER data are also synthetically generated using 17 electrodes placed on the air-ground interface with 1 m spacing between them and acquiring all possible dipole-dipole and Wenner array configurations. Figure 7b shows the electrode positions on the ground. Algorithms that optimize the array configuration for a given field site exist (Stummer et al., 2004; Wilkinson et al., 2006; Loke et al., 2010; Uhlemann et al., 2018). In some situations, Uhlemann et al. (2018) find that a small rather than large data set gives the best inversion results. However, the use of these algorithms depend on the specific exploration site, the mesh size of the domain, and can significantly increase acquisition time. It is worth noting that many of these algorithms depend on the computation of the Jacobian of the ER data. Given the fine mesh discretization of our models (dictated by the GPR forward solver), these algorithms would take a significantly larger amount of computer memory than in the usual ER exploration scenarios. Therefore, we choose our array configurations for their common use in field acquisition and simplicity.

Lastly, the boreholes at locations shown in Figure 7c are used to compare our results from the GPR, ER, and joint inversions for the low- and high-conductivity case.

Noise

We add white noise to our synthetic GPR common-source gathers with amplitude 10% of the standard deviation of each common-source gather (see Figure 8), which amounts to a signal-to-noise ratio (S/N) of 25 dB. We then low-pass the data up to 70% of our Nyquist frequency, which is where most of the noise spectra is shared with our noise-free data. Because the synthetic ER data do not follow a Gaussian distribution, we first cluster the data and then add white noise to each cluster with an amplitude of 10% of the standard deviation of each cluster (see Figure 9). We note that the noisy dipole-dipole array gathers exhibit a significantly lower S/N than the noisy Wenner array gathers, although we still use all of our noisy data for our inversions.

GPR inversions

In Figure 10a, we see the recovered permittivity using just GPR data for the low-conductivity scenario. We see the box correctly imaged and with values close to our true model while the bot-

tom reflector is rightly imaged, but the parameter value is not accurate because of amplitude loss in the data due to attenuation and two-way travel. We also observe low-spatial-frequency artifacts as a result of our surface source illumination with amplitudes dependent on the S/N: With larger noise levels, the artifact amplitudes are recovered with a value closer to the permittivity of the box anomaly. For the high-conductivity scenario (Figure 11a), the amplitude loss in the GPR data is even greater yielding speckle artifacts near the box of only 7.5% between the permittivity of the background and the box.

The lack of amplitude information due to attenuation of the GPR data is also appreciated in the recovered conductivities using only the GPR inversion as seen in Figure 12a for the low conductivity and even more so in Figure 13a for the high conductivity. We note that because of the nonuniqueness between the reflectivity caused by conductivity and that caused by permittivity, the GPR conductivity solution detects an artifact apparent boundary at the bottom of the model. High-spatial-frequency artifacts are also present in the recovered low conductivity.

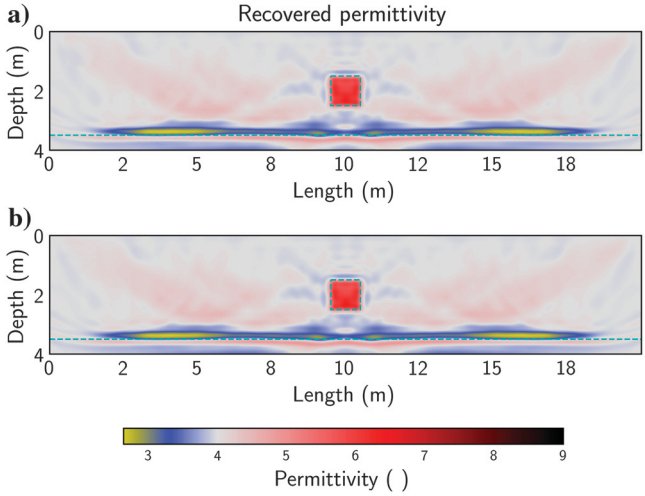

Figure 10. Recovered permittivity for the low-conductivity scenario (a) with just GPR data and (b) with GPR and ER data.

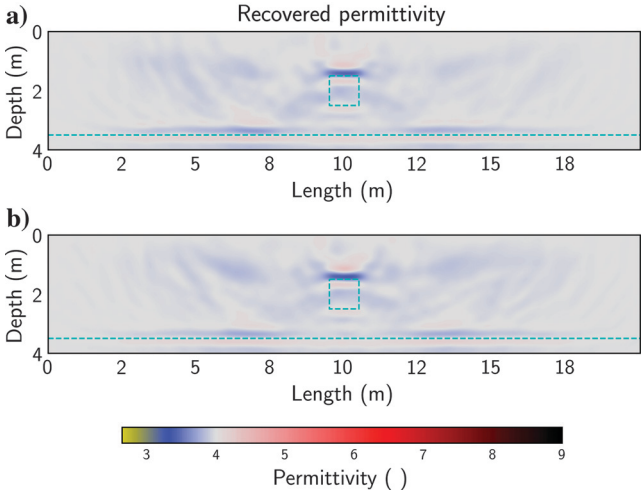

Figure 11. Recovered permittivity for the high-conductivity scenario (a) with just GPR data and (b) with GPR and ER data.

ER inversions

The ER recovered conductivities shown in Figures 12b and 13b for the low- and high-conductivity scenarios tell a different story from the GPR inversions: They have a more accurate amplitude detection and contain more low-spatial frequencies (in the detection of the box and the artifacts of the inversion) and because the ER data are directly and only sensitive to conductivity, they do not contain the bottom reflector. We note, however, that because of our one-sided surface acquisition geometry and the inherent depth resolution of ER, the amplitude of the box decays in depth.

Joint inversions

The joint inversion recovered conductivities for the low and high scenarios are shown in Figures 12c and 13c, respectively. We note improvements in the parameter accuracy and spatial resolution of the recovered conductivities compared to the GPR and ER inversions as well as a better depth resolution of the box. In Table 4, we quantify the improvement of our joint inversion by dividing the zero-lag crosscorrelation of the true and recovered conductivities with the zero-lag autocorrelation of the true conductivities. In the low- and high-conductivity scenarios, we see an improvement over the separate GPR and ER inversions. With respect to the GPR results, we improve by 3% and 5.4% in the low- and high-conductivity scenarios, respectively. With respect to the ER results, we improve by 0.11% in the low- and high-conductivity scenarios.

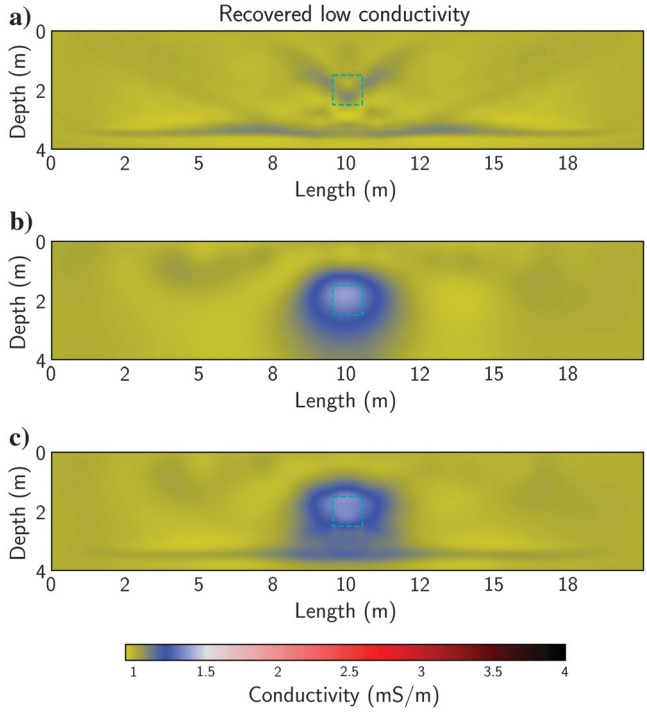

Figure 12. Recovered low conductivity using (a) just GPR data, (b) just ER data, and (c) GPR and ER data. Each inversion was run for 50 iterations.

In Figure 14, we show the recovered conductivity values along the boreholes shown in Figure 7c. Figure 14a and 14c shows the low- and high-conductivity values, respectively, for the borehole at 5 m length. Figure 14b and 14d shows values for the low and high conductivity, respectively, for the borehole located at 10 m in length. In all of the panels, we note the presence of the permittivity reflector in the GPR recovered conductivity. However, in Figure 14a and 14c, this artifact is suppressed in the joint recovered conductivity. This is due to the ER data enhancing the GPR solution by being directly and only sensitive to the conductivity.

However, the effect of the permittivity reflector in the joint recovered conductivity is amplified in Figure 14b and 14d. This is due to the close proximity of the permittivity reflector to the box anomaly and the poor depth resolution of the ER data. In this deep region of the domain, the ER data are not capable of correcting the GPR artifacts reminiscent of the permittivity reflector. However, in the low- and high-conductivity cases, the edges and values of the box anomaly are better resolved in the joint inversion. This enhancement in the box-anomaly boundary is due to the GPR data enhancing the high spatial frequency of the ER solution.

Because of the nonuniqueness of conductivity and permittivity reflections in the GPR data, our joint inversion has the caveat of detecting apparent boundaries in the conductivity solution. We also

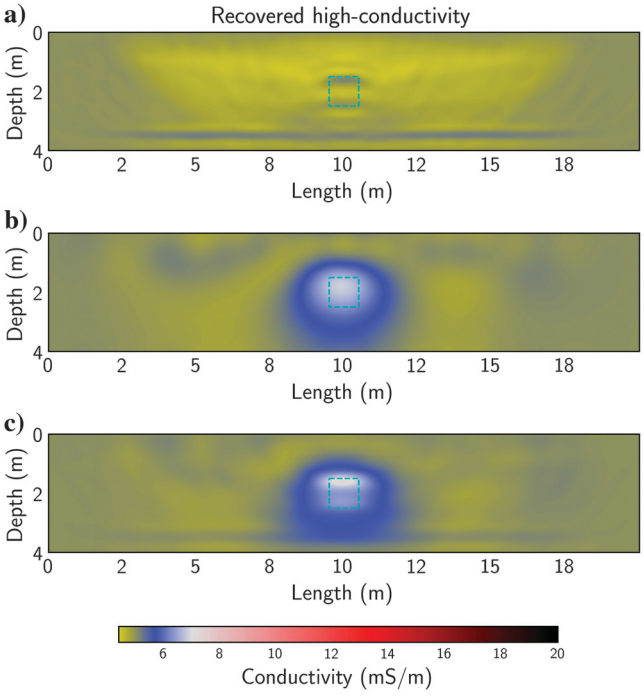

Figure 13. Recovered high conductivity using (a) just GPR data, (b) just ER data, and (c) GPR and ER data. Each inversion was run for 50 iterations.

Table 4. Ratio of the maximum zero-lag crosscorrelation between the recovered and observed parameters for the low- and high-conductivity scenarios.

Inversion	Low σ	High σ
GPR	0.8685	0.8432
ER	0.8964	0.8963
Joint	0.8975	0.8974

[5]Note: Closer to 1 is better. The joint inversion outperforms the GPR and ER recovered conductivities.

Table 5. Frequency dependent and direct current (DC) conductivities at 250 MHz given by the Cole-Cole model.

	Effective (mS/m)	DC (mS/m)	Effective/ DC
Dry sand	4.54	0.45	10.1
Moist sand	6.53	2	3.26
Wet sand	8.06	6.06	1.33
Silty loam	17.3	3.5	4.93
Sandstone with brine	27.2	16.2	1.68
Humus	43.1	19.5	2.21
Laterite	45	9	5
Wet clay	68.4	42.5	1.61
Loess	185	72.3	2.55

[6]Note: Most earth materials present an increase of at most five between DC and (real) the effective conductivity.

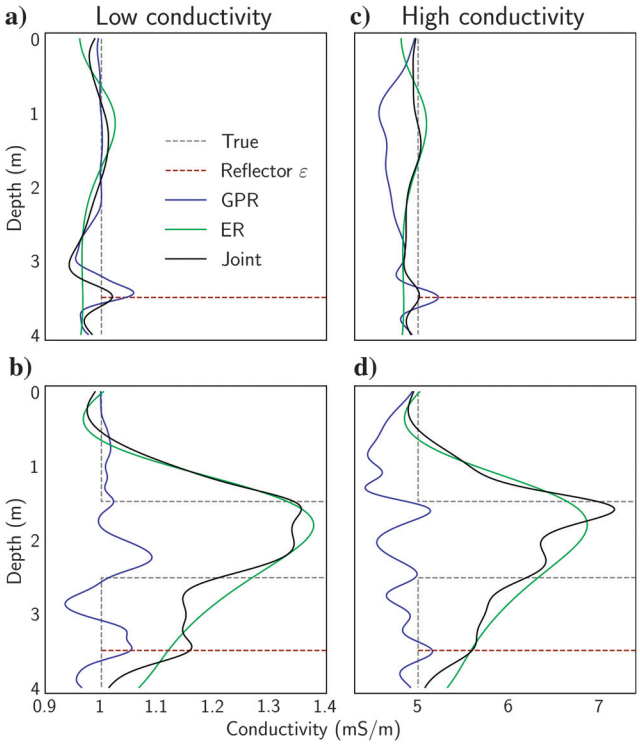

Figure 14. Borehole comparison for the low and high conductivities. True is dashed gray. GPR, ER, and joint recovered conductivities are shown as blue, green, and black, respectively. Dashed red marks the location of the bottom permittivity reflector. The values of the borehole at 5 m length are shown in (a and c). The values of the borehole at 10 m length are shown in (b and d).

note artifacts in our joint inversion conductivities reminiscent of the artifacts in the GPR recovered permittivity around the box anomaly (Figure 10a), although because of our weighting scheme that penalizes $\Delta\boldsymbol{\sigma}_w$ in later iterations, these artifacts diminish the amplitude as the number of iterations increase.

In the low-conductivity scenario, Figure 15a shows that the GPR data dominate $\Delta\boldsymbol{\sigma}$ for the first four iterations resolving sharp boundaries at shallow depths that $\Delta\boldsymbol{\sigma}_{dc}$ is not yet sensitive to. However as the iterations increase, $\Delta\boldsymbol{\sigma}_w$ has contributed enough sensitivity for $\Delta\boldsymbol{\sigma}_{dc}$ to resolve at depth, and so the ER data dominate the inversion resolving the box and smoothing GPR high-spatial-frequency artifacts while still letting $\Delta\boldsymbol{\sigma}_w$ contribute to the inversion. As shown in Figure 15b, the first 20 iterations resolve the data at a faster pace than in later iterations.

Similar to the low-conductivity scenario, the ER data dominates most of the inversion as can be seen in Figure 16a. Figure 16b shows a similar decrease of Θ_{dc} as in Figure 15b, although Θ_w struggles to find a descent direction until the 40th iteration where Θ_w and Θ_{dc} take a final descending stretch.

Because of the lack of information about the subsurface in the GPR data due to strong attenuation, the confidence of Θ_w in resolving the data is weak. The weak confidence of the GPR data is also seen in the small curvature of Θ_w: The changes in Θ_w are small compared to the low-conductivity scenario (Figure 15b), and the step sizes $\alpha^s_{\varepsilon_r}$ flip back and forth between positive and negative values throughout the inversion (not shown). The lack of curvature in Θ_w for the high-conductivity scenario leads us to conclude that incorporating ER sensitivity to $\Delta\boldsymbol{\sigma}_w$ is not enough to resolve permittivity.

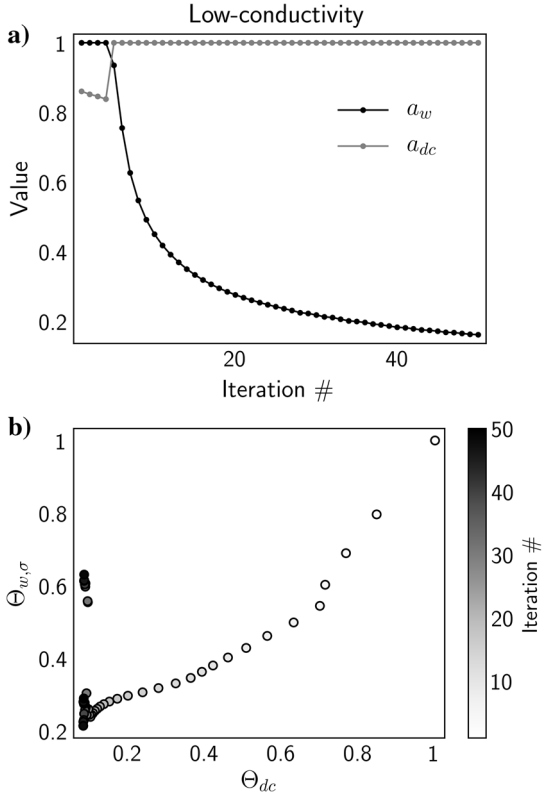

Figure 15. (a) Update weights history over iterations for the low-conductivity scenarios and (b) normalized objective functions history over iterations.

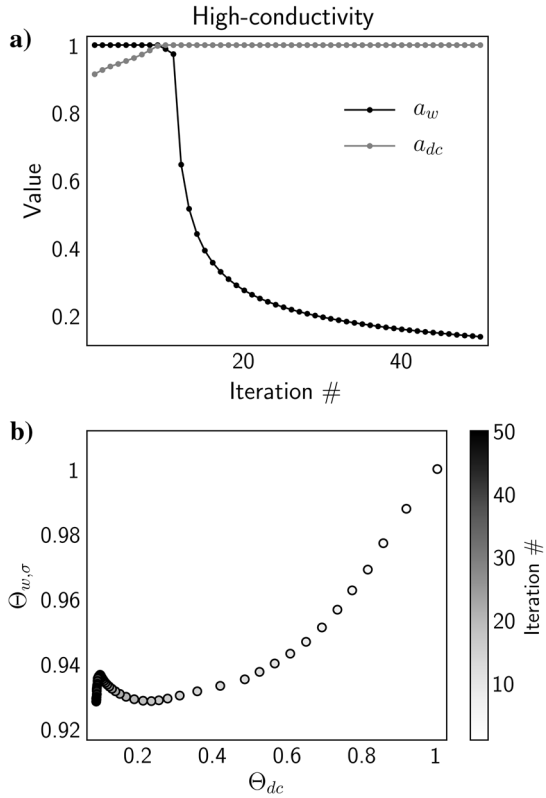

Figure 16. (a) Update weights history over iterations for the high-conductivity scenarios and (b) normalized objective functions history over iterations.

To increase the resolution of permittivity values in the case of high conductivity, four possible solutions could be (1) using the low-frequency information of the GPR in either a stepped frequency approach as Meles et al. (2012), (2) changing the objective function in early iterations as Bozdağ et al. (2011) or Ernst et al. (2007b) to allow for lower frequency content to be imprinted in $\Delta\varepsilon_r$ and $\Delta\boldsymbol{\sigma}_w$, (3) assuming that the permittivity and conductivity geometric features are similar and using a cross-gradient approach as Haber and Gazit (2013) and Gallardo and Meju (2003), or (4) a joint update approach similar to equation 28 where instead of joining the GPR and ER conductivity sensitivities, we join the permittivity ($\Delta\varepsilon_r$) and joint conductivity ($\Delta\boldsymbol{\sigma}$) updates.

In Domenzain et al. (2019), we improve the resolution of our algorithm by incorporating the envelope of the GPR data and using the cross-gradient constraint in a single objective function.

CONCLUSION

We have developed a joint inversion algorithm for recovering subsurface frequency-independent electrical permittivity and conductivity with surface acquisition and no assumed geometry or structure of the target media. Our joint inversion approach enhances the sensitivity of the GPR and ER data by introducing low- and high-spatial-frequency information while honoring the physics of the Maxwell equations. This improves the frequency-independent permittivity and conductivity spatial and amplitude resolution of the target media compared with just GPR or ER inversions. Moreover, we find that GPR effec-

DOI:10.1190/geo2019-0754.1

tively supports ER in regions of low conductivity, whereas ER supports GPR in regions with strong attenuation.

We perform an iterative nonlinear inversion in which the GPR and ER sensitivities are computed with the adjoint method. The GPR and ER sensitivities of the conductivity are joined with an ad-hoc method. The paradigm of our method is to let both sensitivities always contribute to the inversion in proportion to how well their respective data are being resolved in each iteration. Our weighting method makes use of five fixed user-defined values that further regulate the GPR and ER conductivity sensitivities automatically in each iteration. They rely on the physical resolution of the GPR and ER experiments. Because our ad-hoc method to join the GPR and ER sensitivities is based on the value of the objective function values and the physical resolution of our geophysical methods, we suggest that it can be used for joining other geophysical exploration methods in which the physics involved play a similar role, e.g., active source seismic and gravity, which are linked by density.

We assume the subsurface media is linear, isotropic, 2D, and with frequency-independent electrical parameters. In an effort to relax a priori knowledge of the subsurface, we do not use any petrophysical relationships throughout our work. These assumptions were chosen as a compromise between ease of computation cost and relevance with field data scenarios. Moreover, we note that for a variety of earth materials, the direct current (DC) and effective conductivity differ by a factor of less than an order of magnitude. Our assumptions enable us to directly couple the electrical conductivity sensitivities that the GPR and ER data are sensitive to. Although frequency-independent parameters are not true in general, they serve as a starting point for testing our algorithm and motivate the development of forward models and inversion schemes that do take into account the frequency dependency of electrical parameters.

To benchmark our algorithm, we simulate GPR and ER data on two subsurface models, one with low (in the order of 10 mS/m or less) and one with high (in the order of more than 10 mS/m) conductivity. The low-conductivity model was designed to test our algorithm in a case in which the recovered permittivity is sufficiently resolved by the GPR data alone whereas the conductivity is only meaningfully recovered by the ER data. The high-conductivity model was designed to test for a case where the GPR data alone cannot resolve a meaningful image of either permittivity or conductivity. Sources and receivers were placed on the air-ground interface simulating a real-data acquisition scenario for the GPR and ER experiments.

In both cases, our joint inversion approach improves the resolution of spatial dimensions and amplitude of the target conductivity from just the GPR and ER inversions. The spatial detection is measured as a ratio of zero-lag crosscorrelations between the true and recovered parameters. It is improved by 3% and 5.4% with respect to the GPR inversions in the low- and high-conductivity scenarios, respectively, and by 0.11% in both scenarios with respect to the ER inversions.

Because of the nonuniqueness between the permittivity and conductivity reflections in the GPR data, our joint inversion scheme introduces apparent boundaries in the recovered conductivity, which are not corrected with the ER data. High-spatial frequency artifacts of the GPR sensitivity to the conductivity are mapped into our joint inversion solution, although these artifacts can be diminished in amplitude if the inversion is run for more iterations allowing for the low-spatial-frequency ER sensitivity to correct them. In the low- and high-conductivity scenarios, the recovered permittivity is not enhanced by using the ER sensitivity to conductivity, which can be of particular interest in the high-conductivity case in which permittivity is poorly solved by the GPR inversion.

Given the poor amplitude detection of the permittivity in the high-conductivity scenario, approaches to increase the permittivity solution should likely (1) exploit low-frequency content of the GPR data and (2) assume structural similarities of permittivity and conductivity. A possible path to enhance the low-frequency sensitivity of the GPR data could involve changing the objective function of the GPR inversion in early iterations or sequentially increase the frequency content of the GPR data during the inversion. If structural similarities between permittivity and conductivity are assumed, possible paths to accomplish (2) could be joining the conductivity sensitivities of the GPR and ER data in a cross-gradient scheme or with a similar approach as presented in this paper for joining the GPR and ER conductivity sensitivities. In Part 2, we address points (1) and (2) by enhancing our joint inversion with the envelope transform of the GPR data and cross-gradient constraints on permittivity and conductivity. We test these enhancements on the same synthetic models presented here and in a challenging synthetic model based on an alluvial aquifer.

Allowing for deeper spatial sensitivity for the ER experiment is equivalent to using long one-sided surface acquisition. To recover low frequencies and enough amplitude information from the GPR experiment, long one-sided surface acquisition of multioffset data is needed. Given that our joint update for the conductivity assumes that both updates are in the same spatial coordinates and with the same discretization, the cost for computing the GPR and ER forward models is increased from conventional GPR or ER experiments and inversion schemes. As a result, long offsets for both experiments are needed, yielding our approach best suited for shallow subsurface investigation.

Inverting for subsurface electrical properties using full waveform GPR data with data acquired on the surface is a new and emerging method. Choosing to carefully study synthetic examples in which the solution is known enables us to assess the attributes and limitations of our method. This is an important step before using field data with our method because, in general, the solution of subsurface electrical parameters is unknown.

ACKNOWLEDGEMENTS

This work was supported by grants DMS-1418714 and DMS-1720472 given by the National Science Foundation. We would also like to acknowledge the high-performance computing R2 cluster (doi: 10.18122/B2S41H) provided by Boise State University's Research Computing Department.

DATA AND MATERIALS AVAILABILITY

Data associated with this research are available and can be obtained by contacting the corresponding author.

APPENDIX A

FREQUENCY-INDEPENDENT PARAMETERS

In Figure A-1a and A-1b, we present the real part of the frequency-dependent effective conductivity as well as the DC conductivity. These values were computed using the Cole-Cole model with parameters given by Bradford (2007) (for sands and clay), Friel and

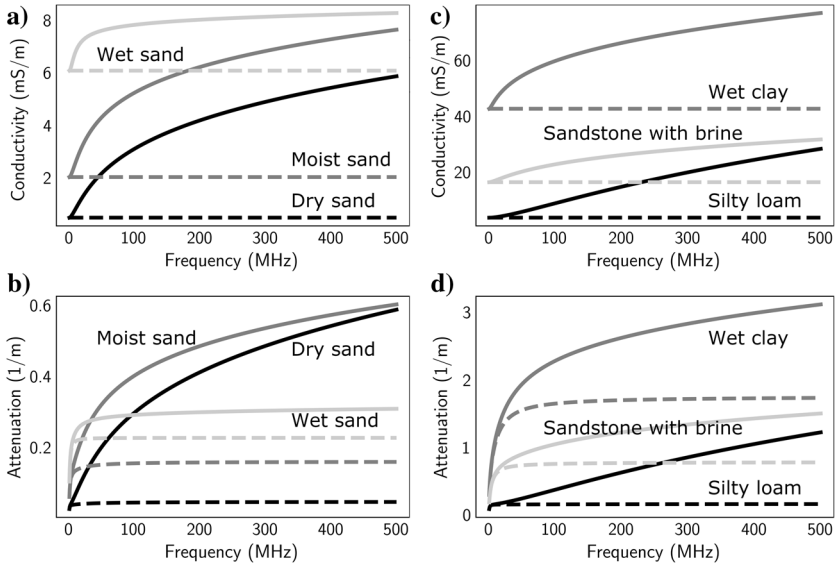

Figure A-1. Frequency-dependent conductivity and attenuation coefficients of various earth materials. The solid and dashed lines represent the (real) effective and DC conductivity, respectively. In (a and b) are low-conductivity materials in which the GPR data have a large S/N. In (c and d) are high-conductivity materials in which GPR data have a low S/N.

Or (1999) (for silty loam), and Taherian et al. (1990) (for sandstone with brine). In general, the more conductive the material, the larger the difference between DC and the effective conductivity. However, the larger the conductivity, the less signal we have in the GPR data. Figure A-1d shows that for high conductivity, the skin factor drops below 1 m as the materials increase in conductivity. We note that for most earth materials, the DC and effective conductivity differ by a factor of less than an order of magnitude. In Table 5, we complete our list of materials with those by Loewer et al. (2017) (for humus, laterite, and loess). We quantify how much this factor is at 250 MHz, and we find that most earth materials differ by a factor of less than 5. Only dry sand (for this particular measured sample) exhibits a factor of 10, although the DC and effective conductivity are still low with 0.45 and 4.5 mS/m, respectively.

We conclude that for most earth materials relevant to GPR applications, assuming frequency-independent parameters is a valid approximation within one order of magnitude.

APPENDIX B

OPTIMALLY PERTURBING

Given a descent direction, finding the right step size is equivalent to traversing the objective function hypersurface in the direction of the gradient $(-a\mathbf{g}^s_{\varepsilon_r})$ starting from our current value of ε_r and finding the value $a = \alpha^s_{\varepsilon_r}$ that minimizes the objective function (Wright and Nocedal, 1999). Traversing the objective function hypersurface is done by perturbing the current value for ε_r with a collection of real numbers a_i. In equation 11, we used the notation $a_i = p_i\kappa_{\varepsilon_r}$ and gave empirical values for p_i. In this section, we find κ_{ε_r}.

To speed up convergence but maintain stability, we perform a descending search for κ_{ε_r}. We start with a large value of κ_{ε_r} and compute the perturbation $\hat{\varepsilon}_r$,

$$\hat{\varepsilon}_r = \varepsilon_r \odot \exp(-\varepsilon_r \odot \kappa_{\varepsilon_r}\mathbf{g}^s_{\varepsilon_r}). \quad \text{(B-1)}$$

We then check if the minimum and maximum values of $\hat{\varepsilon}_r$ lie within our stability velocity region: If they do, we have found κ_{ε_r}; if they do not, we decrease κ_{ε_r} until they do. In practice, once we have found a value of κ_{ε_r} that lies within our stability region, we repeat the search with finer ascending values of κ_{ε_r} to make sure that $\hat{\varepsilon}_r$ is as snug as possible in our velocity interval.

APPENDIX C

ER GRADIENT

Taking the derivative with respect to $\boldsymbol{\sigma}$ and using the chain rule on the ER objective function for one source location,

$$\Theta^s_{dc}(\boldsymbol{\sigma}; \mathbf{s}_{dc}, \mathbf{d}^{o,s}_{dc}) = \frac{\|\mathbf{d}^s_{dc} - \mathbf{d}^{o,s}_{dc}\|_2^2}{\|\mathbf{d}^{o,s}_{dc}\|_2^2}, \quad \text{(C-1)}$$

we have

$$\nabla_\sigma \Theta^s_{dc} = \nabla_{\mathbf{d}_{dc}} \Theta^s_{dc} \cdot \nabla_\sigma \mathbf{d}^s_{dc}, \quad \text{(C-2)}$$

where $\nabla_\sigma \Theta^s_{dc}$ and $\nabla_{\mathbf{d}^s_{dc}} \Theta^s_{dc}$ are vectors of size $1 \times n_x n_z$ and $1 \times n_{\mathbf{d}^s_{dc}}$, respectively (where $n_{\mathbf{d}^s_{dc}}$ is the number of entries in the data), and $\nabla_\sigma \mathbf{d}_{dc}$ is the Jacobian $\mathbf{J}_{dc}$ of $\mathbf{d}_{dc}$, a matrix of size $n_{\mathbf{d}^s_{dc}} \times n_x n_z$. Because of our choice of Θ^s_{dc} to be the sum of square errors, $\nabla_{\mathbf{d}^s_{dc}} \Theta^s_{dc}$ is equal to $\mathbf{e}^{\mathrm{T}}_{dc}$. We make the convention of calling $\mathbf{g}^s_{dc}$ the vertical vector whose entries are the partial derivatives of Θ^s_{dc} with respect to σ; i.e. $\mathbf{g}^s_{dc} = (\nabla_\sigma \Theta^s_{dc})^{\mathrm{T}}$. We now take the transpose of equation C-2,

$$\mathbf{g}^s_{dc} = \mathbf{J}^{\mathrm{T}}_{dc}\mathbf{e}_{dc}. \quad \text{(C-3)}$$

Our task will be to find a different expression for the right side of equation C-3 (Pratt et al., 1998; Domenzain et al., 2017).

Using the product rule on equation 17, we have

$$\mathbf{L}_{dc}\nabla_\sigma \varphi + (\nabla_\sigma \mathbf{L}_{dc})\varphi = 0. \quad \text{(C-4)}$$

We now transpose equation C-4,

$$(\nabla_\sigma \varphi)^{\mathrm{T}}\mathbf{L}^{\mathrm{T}}_{dc} = \mathbf{S}_{dc}, \quad \text{(C-5)}$$

where $\mathbf{S}_{dc} = -((\nabla_\sigma \mathbf{L}_{dc})\varphi)^{\mathrm{T}}$ is a matrix of size $n_x n_z \times n_x n_z$ whose entries are explicitly calculated as a function of $\boldsymbol{\sigma}$, the spatial discretization, and φ. We define the adjoint field $\mathbf{v}_{dc}$ to satisfy

$$\mathbf{L}^{\mathrm{T}}_{dc}\mathbf{v}_{dc} = \mathbf{M}^{\mathrm{T}}_{dc}\mathbf{e}_{dc}, \quad \text{(C-6)}$$

and we multiply equation C-5 on the right side by $\mathbf{v}_{dc}$,

$$\begin{aligned}
(\nabla_\sigma \varphi)^{\mathrm{T}}\mathbf{L}^{\mathrm{T}}_{dc}\mathbf{v}_{dc} &= \mathbf{S}_{dc}\mathbf{v}_{dc},\\
(\nabla_\sigma \varphi)^{\mathrm{T}}\mathbf{M}^{\mathrm{T}}_{dc}\mathbf{e}_{dc} &= \mathbf{S}_{dc}\mathbf{v}_{dc},\\
(\nabla_\sigma \mathbf{d}^s_{dc})^{\mathrm{T}}\mathbf{e}_{dc} &= \mathbf{S}_{dc}\mathbf{v}_{dc},\\
\mathbf{J}^{\mathrm{T}}_{dc}\mathbf{e}_{dc} &= \mathbf{S}_{dc}\mathbf{v}_{dc}, \quad \text{(C-7)}
\end{aligned}$$

where in the second-to-last equality, we have used $\nabla_\sigma \mathbf{d}^s_{dc} = \mathbf{M}_{dc} \nabla_\sigma \varphi$. Finally we write

$$\mathbf{g}^s_{dc} = \mathbf{S}_{dc} \mathbf{v}_{dc}. \tag{C-8}$$

We note that this approach is similar to Pidlisecky et al. (2007), although we have explicitly written an expression for $\mathbf{L}_{dc}$ and $\mathbf{S}_{dc}$ entry by entry rather than as a multiplication of discretized differential operators, which yields full rank on $\mathbf{L}_{dc}$ and $\mathbf{S}_{dc}$ because of the used boundary conditions.

REFERENCES

Babcock, E., and J. H. Bradford, 2015, Reflection waveform inversion of ground-penetrating radar data for characterizing thin and ultrathin layers of nonaqueous phase liquid contaminants in stratified media: Geophysics, **80**, no. 2, H1–H11, doi: 10.1190/geo2014-0037.1.

Beff, L., T. Günther, B. Vandoorne, V. Couvreur, and M. Javaux, 2013, Three-dimensional monitoring of soil water content in a maize field using electrical resistivity tomography: Hydrology and Earth System Sciences, **17**, 595–609, doi: 10.5194/hess-17-595-2013.

Benedetto, A., 2010, Water content evaluation in unsaturated soil using GPR signal analysis in the frequency domain: Journal of Applied Geophysics, **71**, 26–35, doi: 10.1016/j.jappgeo.2010.03.001.

Berenger, J.-P., 1996, Perfectly matched layer for the FDTD solution of wave-structure interaction problems: IEEE Transactions on Antennas and Propagation, **44**, 110–117, doi: 10.1109/8.477535.

Bergmann, P., C. Schmidt-Hattenberger, D. Kiessling, C. Rücker, T. Labitzke, J. Henninges, G. Baumann, and H. Schütt, 2012, Surface-downhole electrical resistivity tomography applied to monitoring of CO_2 storage at Ketzin, Germany: Geophysics, **77**, no. 6, B253–B267, doi: 10.1190/geo2011-0515.1.

Binley, A., G. Cassiani, R. Middleton, and P. Winship, 2002, Vadose zone flow model parameterisation using cross-borehole radar and resistivity imaging: Journal of Hydrology, **267**, 147–159, doi: 10.1016/S0022-1694(02)00146-4.

Bleistein, N., 1986, Two-and-one-half dimensional in-plane wave propagation: Geophysical Prospecting, **34**, 686–703, doi: 10.1111/j.1365-2478.1986.tb00488.x.

Bozdağ, E., J. Trampert, and J. Tromp, 2011, Misfit functions for full waveform inversion based on instantaneous phase and envelope measurements: Geophysical Journal International, **185**, 845–870, doi: 10.1111/j.1365-246X.2011.04970.x.

Bradford, J. H., 2006, Applying reflection tomography in the postmigration domain to multifold ground-penetrating radar data: Geophysics, **71**, no. 1, K1–K8, doi: 10.1190/1.2159051.

Bradford, J. H., 2007, Frequency-dependent attenuation analysis of ground-penetrating radar data: Geophysics, **72**, no. 3, J7–J16, doi: 10.1190/1.2710183.

Bradford, J. H., and J. C. Deeds, 2006, Ground-penetrating radar theory and application of thin-bed offset-dependent reflectivity: Geophysics, **71**, no. 3, K47–K57, doi: 10.1190/1.2194524.

Bradford, J. H., J. T. Harper, and J. Brown, 2009, Complex dielectric permittivity measurements from ground-penetrating radar data to estimate snow liquid water content in the pendular regime: Water Resources Research, **45**, W08403, doi: 10.1029/2009WR008959.

Brunet, P., R. Clément, and C. Bouvier, 2010, Monitoring soil water content and deficit using electrical resistivity tomography (ERT) — a case study in the Cevennes area, France: Journal of Hydrology, **380**, 146–153, doi: 10.1016/j.jhydrol.2009.10.032.

Carrigan, C. R., X. Yang, D. J. LaBrecque, D. Larsen, D. Freeman, A. L. Ramirez, W. Daily, R. Aines, R. Newmark, J. Friedmann, and S. Hovorka, 2013, Electrical resistance tomographic monitoring of CO_2 movement in deep geologic reservoirs: International Journal of Greenhouse Gas Control, **18**, 401–408, doi: 10.1016/j.ijggc.2013.04.016.

Courant, R., K. Friedrichs, and H. Lewy, 1967, On the partial difference equations of mathematical physics: IBM Journal of Research and Development, **11**, 215–234, doi: 10.1147/rd.112.0215.

Cucker, F., and S. Smale, 2007, Emergent behavior in flocks: IEEE Transactions on Automatic Control, **52**, 852–862, doi: 10.1109/TAC.2007.895842.

Dey, A., and H. Morrison, 1979, Resistivity modelling for arbitrarily shaped two-dimensional structures: Geophysical Prospecting, **27**, 106–136, doi: 10.1111/j.1365-2478.1979.tb00961.x.

Dogan, M., R. L. Van Dam, G. C. Bohling, J. J. Butler, and D. W. Hyndman, 2011, Hydrostratigraphic analysis of the made site with full-resolution GPR and direct-push hydraulic profiling: Geophysical Research Letters, **38**, L06405, doi: 10.1029/2010GL046439.

Domenzain, D., 2020, Joint inversion of GPR and ER data: PhD thesis, Boise State University.

Domenzain, D., J. Bradford, and J. Mead, 2017, Imaging by joint inversion of electromagnetic waves and DC currents: Presented at the SIAM Mathematical and Computational issues in the Geosciences.

Domenzain, D., J. Bradford, and J. Mead, 2019, Joint inversion of full-waveform GPR and ER data — Part 2: Enhancing low frequencies with the envelope transform and cross-gradients: Geophysics, **85**, this issue, doi: 10.1190/geo2019-0755.1.

Ernst, J. R., A. G. Green, H. Maurer, and K. Holliger, 2007a, Application of a new 2D time-domain full-waveform inversion scheme to crosshole radar data: Geophysics, **72**, no. 5, J53–J64, doi: 10.1190/1.2761848.

Ernst, J. R., H. Maurer, A. G. Green, and K. Holliger, 2007b, Full-waveform inversion of crosshole radar data based on 2-D finite-difference time-domain solutions of Maxwell's equations: IEEE Transactions on Geoscience and Remote Sensing, **45**, 2807–2828, doi: 10.1109/TGRS.2007.901048.

Fikos, I., G. Vargemezis, J. Zlotnicki, J. Puertollano, P. Alanis, R. Pigtain, E. Villacorte, G. Malipot, and Y. Sasai, 2012, Electrical resistivity tomography study of Taal volcano hydrothermal system, Philippines: Bulletin of Volcanology, **74**, 1821–1831, doi: 10.1007/s00445-012-0638-5.

Friel, R., and D. Or, 1999, Frequency analysis of time-domain reflectometry (TDR) with application to dielectric spectroscopy of soil constituents: Geophysics, **64**, 707–718, doi: 10.1190/1.1444580.

Gallardo, L. A., and M. A. Meju, 2003, Characterization of heterogeneous near-surface materials by joint 2D inversion of DC resistivity and seismic data: Geophysical Research Letters, **30**, 1658, doi: 10.1029/2003GL017370.

Ghose, R., and E. Slob, 2006, Quantitative integration of seismic and GPR reflections to derive unique estimates for water saturation and porosity in subsoil: Geophysical Research Letters, **33**, L05404, doi: 10.1029/2005GL025376.

Giannakis, I., A. Giannopoulos, and C. Warren, 2015, A realistic FDTD numerical modeling framework of ground penetrating radar for landmine detection: IEEE Journal of Selected Topics in Applied Earth Observations and Remote Sensing, **9**, 37–51, doi: 10.1109/JSTARS.2015.2468597

Gueting, N., T. Vienken, A. Klotzsche, J. van der Kruk, J. Vanderborght, J. Caers, H. Vereecken, and A. Englert, 2017, High resolution aquifer characterization using crosshole GPR full-waveform tomography: Comparison with direct-push and tracer test data: Water Resources Research, **53**, 49–72, doi: 10.1002/2016WR019498.

Ha, T., S. Pyun, and C. Shin, 2006, Efficient electric resistivity inversion using adjoint state of mixed finite-element method for Poisson's equation: Journal of Computational Physics, **214**, 171–186, doi: 10.1016/j.jcp.2005.09.007.

Haber, E., and M. H. Gazit, 2013, Model fusion and joint inversion: Surveys in Geophysics, **34**, 675–695, doi: 10.1007/s10712-013-9232-4.

Haber, E., and D. Oldenburg, 1997, Joint inversion: A structural approach: Inverse Problems, **13**, 63, doi: 10.1088/0266-5611/13/1/006.

Hauck, C., D. V. Mühll, and H. Maurer, 2003, Using DC resistivity tomography to detect and characterize mountain permafrost: Geophysical Prospecting, **51**, 273–284, doi: 10.1046/j.1365-2478.2003.00375.x.

Hermans, T., A. Vandenbohede, L. Lebbe, and F. Nguyen, 2012, A shallow geothermal experiment in a sandy aquifer monitored using electric resistivity tomography: Geophysics, **77**, no. 1, B11–B21, doi: 10.1190/geo2011-0199.1.

Hetrick, H., and J. Mead, 2018, Geophysical imaging of subsurface structures with least squares estimates: Inverse Problems in Science and Engineering, **26**, 1656–1675, doi: 10.1080/17415977.2018.1423682.

Holliger, K., M. Musil, and H. Maurer, 2001, Ray-based amplitude tomography for crosshole georadar data: A numerical assessment: Journal of Applied Geophysics, **47**, 285–298, doi: 10.1016/S0926-9851(01)00072-6.

Jazayeri, S., A. Klotzsche, and S. Kruse, 2018, Improving estimates of buried pipe diameter and infilling material from ground-penetrating radar profiles with full-waveform inversion: Geophysics, **83**, no. 4, H27–H41, doi: 10.1190/geo2017-0617.1.

Johnson, T. C., P. S. Routh, W. Barrash, and M. D. Knoll, 2007, A field comparison of Fresnel zone and ray-based GPR attenuation-difference tomography for time-lapse imaging of electrically anomalous tracer or contaminant plumes: Geophysics, **72**, no. 2, G21–G29, doi: 10.1190/1.2431638.

Jomard, H., T. Lebourg, Y. Guglielmi, and E. Tric, 2010, Electrical imaging of sliding geometry and fluids associated with a deep seated landslide (La Clapière, France): Earth surface processes and landforms: The Journal of the British Geomorphological Research Group, **35**, 588–599, doi: 10.1002/esp.1941.

Kjær, K. H., N. K. Larsen, T. Binder, A. A. Bjørk, O. Eisen, M. A. Fahnestock, S. Funder, A. A. Garde, H. Haack, V. Helm, and M. Houmark-Nielsen, 2018, A large impact crater beneath Hiawatha glacier in northwest Greenland: Science Advances, **4**, eaar8173, doi: 10.1530/ey.16.14.7.

Klotzsche, A., J. van der Kruk, J. Bradford, and H. Vereecken, 2014, Detection of spatially limited high-porosity layers using crosshole GPR signal analysis and full-waveform inversion: Water Resources Research, **50**, 6966–6985, doi: 10.1002/2013WR015177.

Knight, R., 2001, Ground penetrating radar for environmental applications: Annual Review of Earth and Planetary Sciences, **29**, 229–255, doi: 10.1146/annurev.earth.29.1.229.

Kurzmann, A., A. Przebindowska, D. Köhn, and T. Bohlen, 2013, Acoustic full waveform tomography in the presence of attenuation: A sensitivity analysis: Geophysical Journal International, **195**, 985–1000, doi: 10.1093/gji/ggt305.

Lavoué, F., R. Brossier, L. Métivier, S. Garambois, and J. Virieux, 2014, Two-dimensional permittivity and conductivity imaging by full waveform inversion of multioffset GPR data: A frequency-domain quasi-Newton approach: Geophysical Journal International, **197**, 248–268, doi: 10.1093/gji/ggt528.

Linde, N., A. Binley, A. Tryggvason, L. B. Pedersen, and A. Revil, 2006, Improved hydro-geophysical characterization using joint inversion of cross-hole electrical resistance and ground-penetrating radar traveltime data: Water Resources Research, **42**, W12404, doi: 10.1029/2006WR005131.

Linde, N., and J. A. Vrugt, 2013, Distributed soil moisture from crosshole ground-penetrating radar travel times using stochastic inversion: Vadose Zone Journal, **12**, 1–16, doi: 10.2136/vzj2012.0101.

Liu, T., A. Klotzsche, M. Pondkule, H. Vereecken, Y. Su, and J. van der Kruk, 2018, Radius estimation of subsurface cylindrical objects from ground-penetrating-radar data using full-waveform inversion: Geophysics, **83**, no. 6, H43–H54, doi: 10.1190/geo2017-0815.1.

Loewer, M., T. Günther, J. Igel, S. Kruschwitz, T. Martin, and N. Wagner, 2017, Ultrabroad-band electrical spectroscopy of soils and sediments — A combined permittivity and conductivity model: Geophysical Journal International, **210**, 1360–1373, doi: 10.1093/gji/ggx242.

Loke, M. H., and R. Barker, 1996, Rapid least-squares inversion of apparent resistivity pseudosections by a quasi-Newton method 1: Geophysical Prospecting, **44**, 131–152, doi: 10.1111/j.1365-2478.1996.tb00142.x.

Loke, M. H., P. Wilkinson, and J. Chambers, 2010, Fast computation of optimized electrode arrays for 2D resistivity surveys: Computers and Geosciences, **36**, 1414–1426, doi: 10.1016/j.cageo.2010.03.016.

Meles, G. A., S. Greenhalgh, J. Van der Kruk, A. Green, and H. Maurer, 2012, Taming the non-linearity problem in GPR full-waveform inversion for high contrast media: Journal of Applied Geophysics, **78**, 31–43, doi: 10.1016/j.jappgeo.2011.12.001.

Meles, G. A., J. Van der Kruk, S. A. Greenhalgh, J. R. Ernst, H. Maurer, and A. G. Green, 2010, A new vector waveform inversion algorithm for simultaneous updating of conductivity and permittivity parameters from combination crosshole/borehole-to-surface GPR data: IEEE Transactions on Geoscience and Remote Sensing, **48**, 3391–3407, doi: 10.1109/TGRS.2010.2046670.

Moorkamp, M., 2017, Integrating electromagnetic data with other geophysical observations for enhanced imaging of the earth: A tutorial and review: Surveys in Geophysics, **38**, 935–962, doi:10.1007/s10712-017-9413-7.

Ogunbo, J. N., G. Marquis, J. Zhang, and W. Wang, 2018, Joint inversion of seismic travel-time and frequency-domain airborne electromagnetic data for hydrocarbon exploration: Geophysics, **83**, no. 2, U9–U22, doi: 10.1190/geo2017-0112.1.

Parsekian, A. D., L. Slater, and D. Giménez, 2012, Application of ground-penetrating radar to measure near-saturation soil water content in peat soils: Water Resources Research, **48**, W02533, doi: 10.1029/2011WR011303.

Perrone, A., V. Lapenna, and S. Piscitelli, 2014, Electrical resistivity tomography technique for landslide investigation: A review: Earth-Science Reviews, **135**, 65–82, doi: 10.1016/j.earscirev.2014.04.002.

Pica, A., J. Diet, and A. Tarantola, 1990, Nonlinear inversion of seismic reflection data in a laterally invariant medium: Geophysics, **55**, 284–292, doi: 10.1190/1.1442836.

Pidlisecky, A., E. Haber, and R. Knight, 2007, Resinvm3d: A 3D resistivity inversion package: Geophysics, **72**, no. 2, H1–H10, doi: 10.1190/1.2402499.

Pidlisecky, A., and R. Knight, 2008, Fw2_5d: A matlab 2.5-d electrical resistivity modeling code: Computers and Geosciences, **34**, 1645–1654, doi: 10.1016/j.cageo.2008.04.001

Pratt, R. G., 1999, Seismic waveform inversion in the frequency domain — Part 1: Theory and verification in a physical scale model: Geophysics, **64**, 888–901, doi: 10.1190/1.1444597.

Pratt, R. G., C. Shin, and G. Hick, 1998, Gauss-Newton and full Newton methods in frequency-space seismic waveform inversion: Geophysical Journal International, **133**, 341–362, doi: 10.1046/j.1365-246X.1998.00498.x.

Rödder, T., and C. Kneisel, 2012, Permafrost mapping using quasi-3D resistivity imaging, Murtèl, Swiss Alps: Near Surface Geophysics, **10**, 117–127, doi: 10.3997/1873-0604.2011029.

Rumelhart, D. E., G. E. Hinton, and R. J. Williams, 1986, Learning representations by back-propagating errors: Nature, **323**, 533, doi: 10.1038/323533a0

Scapozza, C., C. Lambiel, L. Baron, L. Marescot, and E. Reynard, 2011, Internal structure and permafrost distribution in two alpine periglacial talus slopes, Valais, Swiss Alps: Geomorphology, **132**, 208–221, doi: 10.1016/j.geomorph.2011.05.010.

Schmid, L., A. Heilig, C. Mitterer, J. Schweizer, H. Maurer, R. Okorn, and O. Eisen, 2014, Continuous snowpack monitoring using upward-looking ground-penetrating radar technology: Journal of Glaciology, **60**, 509–525, doi: 10.3189/2014JoG13J084

Sold, L., M. Huss, M. Hoelzle, H. Andereggen, P. C. Joerg, and M. Zemp, 2013, Methodological approaches to infer end-of-winter snow distribution on alpine glaciers: Journal of Glaciology, **59**, 1047–1059, doi: 10.3189/2013JoG13J015.

Spichak, V. V., and O. K. Zakharova, 2015, Electromagnetic geothermometry: Elsevier.

Spitzer, K., 1998, The three-dimensional dc sensitivity for surface and subsurface sources: Geophysical Journal International, **134**, 736–746, doi: 10.1046/j.1365-246x.1998.00592.x.

Stummer, P., H. Maurer, and A. G. Green, 2004, Experimental design: Electrical resistivity data sets that provide optimum subsurface information: Geophysics, **69**, 120–139, doi: 10.1190/1.1649381.

Taherian, M., W. Kenyon, and K. Safinya, 1990, Measurement of dielectric response of water-saturated rocks: Geophysics, **55**, 1530–1541, doi: 10.1190/1.1442804.

Taillandier, C., M. Noble, H. Chauris, and H. Calandra, 2009, First-arrival traveltime tomography based on the adjoint-state method: Geophysics, **74**, no. 6, WCB1–WCB10, doi: 10.1190/1.3250266.

Tarantola, A., 1984, Inversion of seismic reflection data in the acoustic approximation: Geophysics, **49**, 1259–1266, doi: 10.1190/1.1441754.

Uhlemann, S., P. B. Wilkinson, H. Maurer, F. M. Wagner, T. C. Johnson, and J. E. Chambers, 2018, Optimized survey design for electrical resistivity tomography: Combined optimization of measurement configuration and electrode placement: Geophysical Journal International, **214**, 108–121, doi: 10.1093/gji/ggy128.

Wilkinson, P. B., P. I. Meldrum, J. E. Chambers, O. Kuras, and R. D. Ogilvy, 2006, Improved strategies for the automatic selection of optimized sets of electrical resistivity tomography measurement configurations: Geophysical Journal International, **167**, 1119–1126, doi:10.1111/j.1365-246X.2006.03196.x.

Wright, S., and J. Nocedal, 1999, Numerical optimization: Springer Science, **35**, 7.

Xue, Z., J. Sun, S. Fomel, and T. Zhu, 2017, Accelerating full-waveform inversion with attenuation compensation: Geophysics, **83**, no. 1, A13–A20, doi: 10.1190/geo2017-0469.1.

Yee, K., 1966, Numerical solution of initial boundary value problems involving Maxwell's equations in isotropic media: IEEE Transactions on Antennas and Propagation, **14**, 302–307, doi: 10.1109/TAP.1966.1138693.

Zhu, T., and J. M. Harris, 2014, Modeling acoustic wave propagation in heterogeneous attenuating media using decoupled fractional Laplacians: Geophysics, **79**, no. 3, T105–T116, doi: 10.1190/geo2013-0245.1.